Characterization of Chromia Scales Formed in Supercritical Carbon Dioxide

B. A. Pint, K. A. Unocic, R. G. Brese and J. R. Keiser
Materials Science and Technology Division
Oak Ridge National Laboratory, Oak Ridge, TN, USA

Abstract

Initial experimental work at 700°-800°C is in progress to develop a lifetime model for supercritical CO_2 compatibility for the 30 year duty life for high-efficiency concentrated solar power (CSP) applications at >700°C. Nickel-base alloys 282, 740H and 625 and Fe-base alloy 25 are being evaluated in 500-h cycles at 1 and 300 bar, and 10-h cycles in 1 bar industrial grade (IG) CO_2. The alloys showed similar low rates of oxidation in 1 and 300 bar CO_2 in 500-h cycles at 750°C. However, in 10-h cycles, alloy 25 showed accelerated attack at 700° and 750°C. To help improve understanding of these results, transmission electron microscopy cross-sections were used to study scale growth after 1,000 h in 300 bar IG sCO_2. For alloy 25 at 700°C, only a row of carbides was observed beneath a recrystallized surface layer. Similar carbides were not observed after exposure to laboratory air for 1000 h at 700°C. Carbon was detected in the Cr-rich scale formed in both sCO_2 and air and appears to be noise. Similar characterization was performed for 625 and 282 after exposure to 300 bar sCO_2 for 1000 h at 750°C. The scale on 282 is more complicated due to the Al internal oxidation and Ti incorporation into the scale.

Keywords: supercritical carbon dioxide, high temperature oxidation, ex-situ tensile properties

Introduction

There is considerable current interest in supercritical CO_2 (sCO_2) as the working fluid in applications including fossil energy, nuclear energy and concentrated solar power (CSP) [1-6]. Efficiencies over 50% can be achieved with a sCO_2 Brayton cycle operating at >700°C and 200-300 bar (20-30 MPa) [7]. A CSP industry concern is that relatively little materials compatibility work has been performed at temperatures above 700°C [8-13] and none of the exposures have been conducted longer than 1,000 h for a CSP application with a target lifetime of 30 years or more than 100,000 h of hot time operation. Previously, it has been shown that the oxygen partial pressure in sCO_2 is

similar to that in steam [13]. Therefore, typical oxides are able to form on conventional Fe- and Ni-base alloys. Going back to the 1960's work on gas cooled nuclear reactors, the larger concern with CO_2 is the potentially high carbon activity (a_c) at the metal-scale interface due to the low equilibrium oxygen activity at that interface, particularly with a stable Cr_2O_3 scale [14]. Thus, internal carburization is the larger concern. In particular, a central question is if the much higher pressure in sCO_2 results in different behavior than has been observed at ambient pressure or the up to ~40 bar pressures for gas-cooled reactors [15-20].

For temperatures above 700°C, the experience from the U.S. Advanced Ultrasupercritical Steam Consortium (2001-2015) [21] with temperature and pressure goals of 760°C and 345 bar is relevant to the sCO_2 goals. That program found that precipitation-strengthened Ni-base structural alloys like 740H and 282 [22,23] have significant creep strength advantages over solid solution strengthened alloys. For the CSP application, the daily thermal cycling represents a unique requirement that has been briefly studied for CSP Air Brayton applications using 10-h thermal cycles [24,25].

The current project is attempting to address some of these concerns with long-term testing at 300 bar (30 MPa) at 700°-750°C and 10-h and 500-h cycles in ~1 bar (0.1 MPa, ambient) CO_2 with the goal of developing a CSP-relevant lifetime model for components operating in sCO_2 at 700°-800°C. This study focuses on the 700°-750°C results, particularly at longer times, with the 800°C results included elsewhere [26,27]. More in-depth characterization of the reaction products using scanning transmission electron microscopy (STEM) also is reported.

Experimental Procedure

Four structural alloys were studied and their compositions are shown in Table 1. Coupons (~10 x 20 x 1.5mm) with a 600 grit finish were ultrasonically cleaned in acetone and methanol prior to exposure. The 10-h cyclic tests were performed in an automated cyclic rig [28] at 700° and 750°C in industrial grade (IG) CO_2, with <50ppm O_2, <32ppm H_2O with the specimens hung from alumina rods with Pt-Rh wire and 10 min cooling between cycles in laboratory air to <30°C. Gas flow rates were ~100 cc/min or ~0.1cm/s flow rate.

The coupons were placed in an alumina boat in an alumina reaction tube with end caps for the 500-h cycles at 1 atm IG CO_2. The specimens were heated in flowing Ar to 750°C over 4 h to minimize oxidation of the sample prior to exposure to CO_2, held for 500 h in IG CO_2 and cooled in flowing Ar to room temperature. For the 500-h cycles at 300 bar (30 MPa) in IG sCO_2, the experiments were conducted in an autoclave fabricated from alloy 282 [10,13,27] with the specimens suspended on alumina rods with alumina spacers between specimens. The fluid flow rate was ~2-3 ml/min. The autoclave was slowly heated to temperature over several hours (~2°C/min) in sCO_2, held at temperature ±2°C and then cooled in sCO_2 to room temperature by lowering the furnace and using a cooling fan on the autoclave.

Specimen mass change was measured every 500-h cycle or every 160 h in the 10-h cyclic tests using a Mettler Toledo XP205 balance with an accuracy of ~±0.04mg or 0.01mg/cm^2. After exposure, samples were Cu plated before being sectioned and mounted for light microscopy. The STEM specimens were prepared using the focused ion beam (FIB) lift out technique and imaging was carried out using a FEI model Talos F200X STEM with an integrated energy dispersive x-ray system with four silicon drift detectors.

Results

Figure 1 shows specimen mass change data for the specimens exposed in 1 bar IG CO_2 using 10-h cycles. At 700°C, three specimens of each alloy have completed a 4,000 h exposure (i.e. 400 cycles). While the Ni-base alloy specimens showed reproducible, low mass changes, the Fe-base alloy 25 specimens showed accelerated mass gains after ~150 cycles, Figure 1a. Figure 2a shows the thin, Cr-rich scale formed after 1,000 h while Figure 2b shows the duplex, Fe-rich outer scale formed after 4,000 h. This scale structure is typical of Fe-base alloys exposed to H_2O- and CO_2-containing environments [9,17-20]. The 740H and 282 specimens showed reproducible, nearly parabolic behavior, while the three 625 specimens all had a downward slope (i.e. consistent mass loss) for the latter half of the exposure with very similar behavior. This slight mass loss appears more consistent with an evaporation mechanism than scale spallation of such a thin oxide.

Cross-sections of 625 specimens at 1,000 and 4,000 h are shown in Figures 2c and 2d, respectively. A thin oxide formed after 1,000 h. Some oxide nodules appeared to form after the 4,000 h exposure, but a separation between the specimen and the Cu-plating made it difficult to clearly see the reaction product in Figure 2d. Both 740H and 282 show internal oxidation (Figures 2e-2h) due to the presence of Al and Ti in these alloys, Table 1. The deeper oxide penetrations for 282 reflect the higher Al and Ti contents in this alloy and explain the higher mass gains in Figure 1a. This is similar to observations in steam oxidation for these alloys [29,30].

The exposures at 750°C are continuing to longer times with three specimens of each alloy exposed for >4,000 h, Figure 1b. Similar to the results at 700°C, the alloy 282 specimens showed the highest mass gains and the 625 specimens exhibited a slight mass loss after ~100 cycles. The alloy 25 specimens again showed increased mass gain after ~200 cycles. Characterization of specimens stopped at 1,000 h at 750°C has been reported elsewhere [26,27].

Figure 3 shows mass change data in 300 bar IG sCO_2. At 700°C, 6 specimens of each alloy were exposed while 10 specimens of each alloy were exposed at 750°C. Box and whisker plots indicate the distribution of measurements and the median values are connected by solid lines. At 700°C, two specimens of each alloy were removed at 1,000 h and the four remaining specimens were exposed for another 1,000 h, Figure 3a. Unlike in the cyclic testing, the alloy 25 specimens showed no signs of accelerated attack and the 625 specimens showed no signs of mass loss. The alloy 282 specimens again showed the highest mass gain and the other 3 alloys showed similar mass gains. The 700°C mass change data are supported by the cross-sections after 1,000 and 2,000 h in Figure 4. Thin protective oxides were noted with occasional small nodules observed for the alloy 25 specimen at 2000 h. The internal oxidation was much more distinctive for the 282 specimens, Figures 4g and 4h, consistent with the mass change data.

Figure 3b shows the mass gain data for 750°C where the specimens have completed nine, 500-h cycles. Unlike the 750°C cyclic testing in Figure 1b, the 625 specimens did not lose mass and the alloy 25 specimens have not shown significant increases in mass. However, the mass gains

for the alloy 25 specimens are similar to those for the 740H specimens. Consistent with all of the other conditions, the alloy 282 specimens showed the highest mass gains.

Specimens were removed from this experiment at 1,000, 2,500 and 4,000 h for characterization and cross-sections after 1,000 and 4,000 h are shown in Figure 5. Consistent with the other observations, internal oxidation was observed for the 740H and 282 specimens, that increased in depth and volume with time, Figures 5e-5h. However, in this case, the alloy 25 specimen retained a relatively thin oxide after 4,000 h, Figure 5b. An unusually thick region of the scale on alloy 625 is shown in Figure 5d.

With the available data, parabolic rate constants were fit (R^2 values all 0.975 or higher) to the median data in Figure 3 using the standard method [31]. Figure 6 shows an Arrhenius plot of the measured rate constants for the four alloys in the two experiments. Data for 800°C that was reported elsewhere also is included [26,27]. No rate constants could be calculated for the 625 specimens that lost mass in the cyclic tests. The metric for the project was for the rates to be below $5x10^{-13}$ $g^2cm^{-4}s^{-1}$ where the mass gain after 100,000 h would be ~13 mg/cm^2 and the oxide less than 100µm. The rates for alloy 25 specimens in the cyclic testing do not meet the metric as relatively fast-growing Fe-rich oxides formed. However, in all of the other cases, particularly in 300 bar IG sCO_2, the measured rates are well below the metric and tend to be fairly similar. For alloy 25 in sCO_2, the rate at 700°C was slightly higher than the rate at 750°C and fitting the 3 rates resulted in an unrealistically low activation energy.

The two experiments differ in both CO_2 pressure and cycle frequency. In order to better understand these two parameters, a third experiment was conducted at 750°C using 500-h cycles and 1 bar IG CO_2. Dashed lines in Figure 3b show the median mass gain values for 8 samples of each alloy. (The boxes are not shown for clarity.) Nine 500-h cycles have been performed and the mass gains for the Ni-base alloys 625, 740H and 282 are all remarkably similar to the mass gains in 300 bar sCO_2. In Figure 6, the rates for these experiments are shown with squares, all of which are very similar to the rates in the other experiments. For the alloy 25 specimens, the mass gains were lower. For the alloy 625 specimens, the rate was slightly higher in 1 bar IG CO_2, Figure

6. Characterization of the 500-h cycle, 1 bar CO_2 reaction products after 1,000 h was presented elsewhere [26]. Figure 7 shows a comparison of cross-sections of the specimens removed after 2,500 h in 1 and 300 bar. Consistent with the mass change data, the oxide scales in the two environments appear very similar. A gap between the oxide and the copper plating in Figure 7b makes it difficult to see the thin oxide on the alloy 25 sample.

In order to better understand the behavior of alloy 25, a TEM section was made from the specimen exposed for 1,000 h in 300 bar sCO_2 at 700°C, Figure 8a. Consistent with the mass gain, the scale was very thin, <0.5μm. The most distinctive feature in the bright field STEM image is the recrystallization zone beneath the scale, likely caused by polishing the specimen. Another prominent feature is a row of precipitates beneath the recrystallization zone, about 2μm from the metal-scale interface. In Figure 9, a line profile at a slightly higher magnification shows these precipitates to be carbides (primarily containing Cr) and they were identified by selected area diffraction as $M_{23}C_6$. Figure 10 shows EDS maps of the scale, showing a Cr-rich scale with an underlying layer of silica (Figure 10e) and a Mo-rich precipitate at the metal-scale interface (Figure 10h). Very little Fe was present in the scale after this exposure (Figure 10f) and only small regions of the scale contained Mn (Figure 10g). Figure 10d appears to show C enriched in the scale. However, with the C signal, there is always a concern that the C may be contamination from the TEM specimen preparation process.

To be certain that the carbides seen in Figures 8a and 9 were due to the sCO_2 environment, an alloy 25 specimen was oxidized isothermally for 1,000 h in laboratory air at 700°C. Figure 8b shows the STEM bright field image with a similar thin oxide and recrystallization zone as the specimen oxidized in sCO_2. However, no row of carbides was observed. Based on the maps in Figure 11, the scale is primarily a Cr-rich oxide and the larger, faceted grains appear to be rich in Mn (Figure 11g). In the region that was mapped, no silica layer was observed at the metal-scale interface (Figure 11e). Also, this TEM FIB specimen was inadvertently made with a deposited C layer instead of a W layer so the C map in Figure 11d shows a high C level. Figure 12 compares line profiles taken across both scales. The Cr levels were very similar with a slight Cr depletion

to ~19%Cr detected at the metal-scale interface for both alloys. (In both cases, the Cr depletion depth was ~2μm, similar to the depth of the recrystallization zone.) Only the sCO_2 specimen formed a silica inner oxide layer as indicated by the Si line profiles. Most importantly, the C signal in both specimens was similar. Therefore, the apparent C enrichment in the scale formed in sCO_2 indicated in Figures 9b and 10d was not confirmed. A second FIB specimen of the scale formed in air with a W deposit showed a similar C signal in the scale.

Figures 13 and 14 compare the oxides formed on alloys 625 and 282 after 1,000 h at 750°C in 300 bar sCO_2. For these Ni-base alloys that did not show breakaway oxidation, 750°C was chosen because longer-term exposures will focus on this temperature. Figure 13a shows the scale formed on the alloy 625 specimens in sCO_2. With the higher exposure temperature, the scale is somewhat thicker but is still a fine-grained Cr-rich oxide. Figure 13b shows a line profile through the scale and underlying alloy. No strong C enrichment or carbide formation was observed. Similar to prior exposures, a Nb- and Mo-rich phase was observed adjacent to the scale [32]. Chromium depletion was observed in the underlying metal to ~12% and Si enrichment was observed in the oxide near the metal, suggesting an SiO_2 underlayer. Figure 14a shows the more complex oxide formed on the alloy 282 specimen. Voids were observed beneath the Cr-rich scale. The reaction product is more complicated because of the Al and Ti incorporation. The accompanying maps of this region (Figures 14b-14g) show that Al oxide formed internally (Figure 14d) as has been shown in all of the conditions described above. In contrast, Ti-rich oxides were observed both at the metal- and gas-scale interfaces (Figure 14e). Some C enrichment was observed, but it could be noise or contamination (Figure 14f). The Ni map in Figure 14g suggests some metal particles may have been incorporated into the growing scale.

Discussion

Four alloys were selected for this study based on industry input. The three Ni-base alloys have shown low reaction rates and appear to be good candidates for this application. The Fe-base alloy 25 represents a less expensive option and perhaps is being evaluated at temperatures above its temperature capabilities. The typical steam boiler requirement is for creep rupture life of 100,000 h at a stress of 100 MPa [21], which would restrict this alloy below 700°C. Nevertheless, the faster oxidation rate at longer exposure times in 10-h cycles at 700° and 750°C (Figure 1) was somewhat surprising, especially based on the thin reaction products after 1,000 h exposures (e.g. Figure 2a) [26,27]. The accelerated oxidation appears to be caused by the 10-h thermal cycling in the presence of CO_2 as longer-term exposures in 500-h exposures at 700° and 750°C did not show a similar acceleration, Figure 3. Characterization of the longer-term specimens at 750°C in 10-h cycles has not been performed yet as these specimens are still in test. Currently, more extensive characterization is being performed on the longer-term specimens completed in other conditions.

Previously, based on only 500 h exposures, it was concluded that pressure did not appear to play a significant role in the CO_2 oxidation behavior [13]. The current 4,500 h results at 750°C (Figure 3b) appear to confirm this hypothesis and similar rates were observed at both 1 and 300 bar IG CO_2. If pressure does not play a significant role, then the large database generated for CO_2-cooled nuclear reactors (1-20kh exposures) [33-35] might be utilized as well as the extensive work at 1 bar for a variety of applications including solid oxide fuel cells and oxy-fired coal combustion [18,20,36-38]. However, none of the older work would have considered newer alloys like 740H and 282 and even the more recent work tends to focus on Fe-base alloys, which are more susceptible than Ni-base alloys to internal carburization in these environments [9].

Because of the thin reaction products, SEM and microprobe have not been particularly useful in characterization and TEM was selected. Based on the initial characterization of alloy 25, it became clear that comparisons to air- or O_2-grown oxides are needed to fully understand the role of CO_2. The presence of carbides, Figure 9, in carbide-strengthened alloy 25 is not necessarily due to the environment. However, their absence in the air-oxidized specimen does suggest that the environment played a role. Thus, comparison experiments are beginning at 750°C in laboratory

air in 500-h cycles and in dry O_2 in 10-h cycles. An earlier comparison at 800°C in dry air for 1,000 h in 10-h cycles showed similar reaction rates as the IG CO_2 results with no indication of spallation in either environment [26].

Unfortunately, the STEM/EDS results failed to identify if C was present in the sCO_2-grown scales, Figure 12. Future work will include glow discharge, optical emission spectroscopy (GD-OES) and x-ray photoelectron spectroscopy to try to identify C in these scales. Previous TEM studies found an amorphous C layer at the metal-scale interface at 550°C [11,39]. Nothing similar was observed in this study for specimens exposed at 700°-750°C.

The Ni-base alloys characterized in Figures 13 and 14 after exposure to sCO_2 at 750°C showed no signs of C ingress. Previously it was concluded that Ni-base alloys should be more resistant to internal carburization in sCO_2 because of their lower C solubility [9]. Another strategy to limit internal carburization is the use of alumina-forming alloys. Alumina-forming alloys have been included in prior studies [10,13]. However, these alloys typically do not have sufficient mechanical properties or ASME boiler code approval for use in these applications. An additional concern for sCO_2 heat exchangers is that alumina-forming alloys need to operate over a wide temperature range and may struggle to form alumina at low (>600°C) temperatures.

Recent work suggested the need to examine both stress and the sCO_2 environment [9]. Currently, these four alloys are being creep rupture tested in pressurized air and sCO_2 to determine any lifetime debit due to sCO_2. Finally, all of these experiments were conducted in IG CO_2. It is not known how the potentially higher impurities may affect these results. Additional experiments will begin soon at 750°C using research grade CO_2 (>5ppm H_2O, >5 ppm O_2) at 1 and 300 bar to compare to these results to explore the role of minor impurities. For direct-fired concepts [5], experiments are planned to explore the effect of much higher O_2 and H_2O levels at 300 bar and 750°C.

Summary

Alloys 625, 740H, 282 and Fe-base alloy 25 are being evaluated in 500-h cycles at 1 bar and 300 bar in industrial grade sCO_2, and 10-h cycles in 1 bar CO_2 at 700° and 750°C in order to develop a lifetime model for high efficiency CSP applications. Mass change data has shown that these alloys show low rate constants below the performance metric for 100,000 h lifetime and CO_2 pressure has little effect on the reaction rates. The exception was alloy 25, which showed accelerated mass gain in 10-h cycles at 700° and 750°C in 1 bar CO_2. Characterization of the reaction products using transmission electron microscopy (TEM) did not detect any significant C ingress after exposure to 300 bar sCO_2 for 1000 h. A row of Cr-rich carbides was observed in alloy 25 exposed at 700°C to sCO_2 but no similar carbides were exposed after a similar exposure in laboratory air. There was no clear indication of higher C in the Cr-rich scale formed in sCO_2 in the TEM cross section as high C levels were detected in scales formed in both sCO_2 and air. The scale formed on 282 after exposure to 300 bar sCO_2 for 1000 h was very complicated due to the Al internal oxidation and Ti incorporation into the Cr-rich scale. Characterization of specimens exposed at longer times will focus on alloy 25.

Acknowledgments

The author would like to thank M. Howell, M. Stephens, G. Garner, T. Lowe and T. Jordan at ORNL for assistance with the experimental work, and M. J. Lance and L. F. Allard for comments on the manuscript. The authors appreciate the contributions of our research team members: Brayton Energy, LLC, Special Metals, Haynes International and Sandvik and the input of others from the CSP/sCO_2 industry. This research was funded by the SunShot Initiative under the U.S. Department of Energy's Office of Energy Efficiency and Renewable Energy, Solar Energy Technology Program: SuNLaMP award number DE-EE0001556.

References

1. V. Dostal, P. Hejzlar and M. J. Driscoll, "High-Performance Supercritical Carbon Dioxide Cycle for Next-Generation Nuclear Reactors," Nuclear Technology, 154 (3) (2006) 265-282.

2. X. R. Zhang, H. Yamaguchi, D. Uneno, K. Fujima, M. Enomoto, N. Sawada, "Analysis of a novel solar energy-powered Rankine cycle for combined power and heat generation using supercritical carbon dioxide," Renewable Energy, 31 (2006) 1839-1854.
3. H. Chen, D. Y. Goswami and E. K. Stefanakos, "A review of thermodynamic cycles and working fluids for the conversion of low-grade heat," Renewable & Sustainable Energy Reviews 14 (2010) 3059-3067.
4. B. D. Iverson, T. M. Conboy, J. J. Pasch and A. M. Kruizenga, "Supercritical CO_2 Brayton cycles for solar-thermal energy," Applied Energy, 111 (2013) 957-970.
5. R. J. Allam, M. R. Palmer, G. W. Brown Jr., J. Fetvedt, D. Freed, H. Nomoto, M. Itoh, N. Okita, C. Jones Jr., "High efficiency and low cost of electricity generation from fossil fuels while eliminating atmospheric emissions, including carbon dioxide," Energy Procedia 37 (2013) 1135–1149.
6. V. T. Cheang, R. A. Hedderwick, C. McGregor, "Benchmarking supercritical carbon dioxide cycles against steam Rankine cycles for Concentrated Solar Power," Solar Energy, 113 (2015) 199-211.
7. E. G. Feher, "The Supercritical Thermodynamic Power Cycle," Energy Conversion, 8 (1968) 85-90.
8. C. H. Oh, T. Lillo, W. Windes, T. Totemeier, B. Ward, R. Moore and R. Barner, "Development of a Supercritical Carbon Dioxide Brayton Cycle: Improving VHTR Efficiency and Testing Material Compatibility," Idaho National Laboratory Report INL/EXT-06-01271, 2006.
9. R. I. Olivares, D. J. Young, P. Marvig and W. Stein, "Alloys SS316 and Hastelloy-C276 in Supercritical CO_2 at High Temperature," Oxid. Met. 84 (2015) 585–606.
10. B. A. Pint and J. R. Keiser, "Initial Assessment of Ni-Base Alloy Performance in 0.1 MPa and Supercritical CO_2," JOM 67(11) (2015) 2615-2620.
11. V. Dheeradhada, A. Thatte, M. Karadge and M Drobnjak, "Corrosion of Supercritical CO_2 Turbomachinery Components," in Proceedings of the EPRI International Conference on Corrosion in Power Plants, Oct. 2016, San Diego, CA.
12. J. Mahaffey, D. Adam, M. Anderson and K. Sridharan, (2016) "Effect of Oxygen Impurity on Corrosion in Supercritical CO_2 Environments," in Proceedings of the 5th International Symposium on Supercritical CO_2 Power Cycles, San Antonio, TX, March 2016, Paper #114.
13. B. A. Pint, R. G. Brese and J. R. Keiser, "Effect of Pressure on Supercritical CO_2 Compatibility of Structural Alloys at 750°C," Materials and Corrosion, 68 (2017) 151-158.
14. C. T. Fujii and R. A. Meussner, "Carburization of Fe-Cr Alloys During Oxidation in Dry Carbon Dioxide," J. Electrochem. Soc., 114 (1967) 435-442.

15. H. E. McCoy, “Type 304 Stainless Steel vs Flowing CO_2 at Atmospheric Pressure and 1100-1800°F,” Corrosion 21 (1965) 84-94
16. W. R. Martin and J. R. Weir, “Influence of Chromium Content on Carburization of Chromium-Nickel-Iron Alloys in Carbon Dioxide,” J. Nucl. Mater. 16 (1965) 19-24.
17. F. Rouillard, F. Charton and G. Moine, “Corrosion Behavior of Different Metallic Materials in Supercritical Carbon Dioxide at 550°C and 250 bars,” Corrosion 67 (9) (2011) 095001.
18. D. J. Young, T. D. Nguyen, P. Felfer, J. Zhang and J. M. Cairney, “Penetration of protective chromia scales by carbon,” Scripta Materialia 77 (2014) 29–32.
19. T. Furukawa and F. Rouillard, “Oxidation and carburizing of FBR structural materials in carbon dioxide,” Progress in Nuclear Energy 82 (2015) 136–141.
20. T. D. Nguyen, J. Q. Zhang and D. J. Young, “Microstructures of chromia scales grown in CO_2,” Mater. High Temp. 32 (2015) 16-21.
21. R. Viswanathan, J. Shingledecker and R. Purgert, “Evaluating Materials Technology for Advanced Ultrasupercritical Coal-Fired Plants,” Power, 154(8) (2010) 41-45.
22. L. M. Pike, “Development of a Fabricable Gamma-Prime (γ’) Strengthened Superalloy,” in Superalloys 2008, R. C. Reed et al. eds TMS, Warrendale, PA, 2008, p.191-200.
23. J. P. Shingledecker and G. M. Pharr, “Testing and Analysis of Full-Scale Creep-Rupture Experiments on Inconel Alloy 740 Cold-Formed Tubing,” J. Mater. Eng. Performance, 22 (2013) 454-462.
24. B. A. Pint, “The Future of Alumina-Forming Alloys: Challenges and Applications for Power Generation,” Material Science Forum 696 (2011) 57-62.
25. B. A. Pint, B. N. Anderson, W. J. Matthews, C. Waldhelm and W. Treece, “Evaluation of NiCrAl Foil for a Concentrated Solar Power Application,” ASME Paper #GT2013-94939, presented at the International Gas Turbine & Aeroengine Congress & Exhibition, San Antonio, TX, June 3-7, 2013.
26. R. G. Brese, J. R. Keiser and B. A. Pint, “Effect of Thermal Cycling on Compatibility in CO_2 for Concentrated Solar Power Applications,” Oxidation of Metals, 87 (2017) 631-642.
27. B. A. Pint, R. Brese and J. R. Keiser, (2017) “Effect of Pressure and Thermal Cycling on Compatibility in CO_2 for Concentrated Solar Power Applications,” ASME Paper #GT2017-65066, for the International Gas Turbine & Aeroengine Congress & Exhibition, Charlotte, NC, June 26-30, 2017.
28. B. A. Pint, P. F. Tortorelli and I. G. Wright, "Effect of Cycle Frequency on High Temperature Oxidation Behavior of Alumina-Forming Alloys," Oxidation of Metals 58 (2002) 73-101.

29. E. Essuman, L. R. Walker, P. J. Maziasz and B. A. Pint, “Oxidation Behavior of Cast Ni-Cr Alloys in Steam at 800°C,” Materials Science and Technology, 29 (2013) 822-827.
30. B. A. Pint and B. P. Thiesing, (2015) “Effect of Environment on the Oxidation Behavior of Commercial and Model Ni-Base Alloys,” NACE Paper C2015-5919, Houston, TX, presented at NACE Corrosion 2015, Dallas, TX, March 2015.
31. B. Pieraggi, "Calculations of Parabolic Reaction Rate Constants," Oxid. Met., 27 (1987) 177-85.
32. A. Chyrkin, P. Huczkowski, V. Shemet, L. Singheiser and W. J. Quadakkers, “Sub-Scale Depletion and Enrichment Processes During High Temperature Oxidation of the Nickel Base Alloy 625 in the Temperature Range 900-1000°C,” Oxid. Met. 75 (2011) 143-166.
33. H. E. Evans, D. A. Hilton and R. A. Holm, “Chromium-Depleted Zones and the Oxidation Process in Stainless Steels,” Oxid. Met. 10 (1976) 149-161.
34. J. C. P. Garrett, J. T. Crook, S. K. Lister, P. J. Nolan and J. A. Twelves, “Factors in the Oxidation Assessment of AISI Type 310 Steels in High Pressure Carbon Dioxide,” Corrosion Science 22 (1982) 37-50.
35. Y. Gong, D. J. Young, P. Kontis, Y. L. Chiu, H. Larsson, A. Shin, J. M. Pearson, M. P. Moody and R. C. Reed, “On the breakaway oxidation of Fe9Cr1Mo steel in high pressure CO_2,” Acta Materialia 130 (2017) 361-374.
36. G. H. Meier, W. C. Coons and R. A. Perkins, “Corrosion of Iron-, Nickel- and Cobalt-Base Alloys in Atmospheres Containing Carbon and Oxygen,” Oxidation of Metals 17 (1982) 235-262.
37. J. Pirón Abellán, T. Olszewski, G. H. Meier, L. Singheiser and W. J. Quadakkers, “The Oxidation Behaviour of the 9% Cr Steel P92 in CO_2- and H_2O-rich gases relevant to oxyfuel environments,” Int. J. Mat. Res. 101 (2010) 287-299.
38. T. Gheno, D. Monceau, J. Zhang and D. J. Young, “Carburisation of Ferritic Fe-Cr Alloys by Low Carbon Activity Gases,” Corros. Sci., 53 (2011) 2767-2777.
39. H. J. Lee, H. Kim, S. H. Kim and C. Jang, “Corrosion and carburization behavior of chromia-forming heat resistant alloys in a high-temperature supercritical-carbon dioxide environment,” Corrosion Science 99 (2015) 227–239.

Figure and Table Captions

Figure 1. Specimen mass gain as a function of cumulative exposure time using 10-h cycles in 1 bar IG CO_2 at (a) 700°C (b) 750°C.

Figure 2. Light microscopy of polished cross-sections after (a,c,e,g) 1000 h and (b,d,f,h) 4000 h exposures in 1 bar IG CO_2 at 700°C (a-b) alloy 25, (c-d) 625, (e,f) 740H and (g,h) 282.

Figure 3. Specimen mass gain as a function of exposure time in 300 bar IG CO_2 at (a) 700°C and (b) 750°C. The whiskers show the maximum and minimum values measured for 6-10 specimens at each temperature and the boxes note the 25% and 75% values. The solid lines connect the median values. The dashed lines in (b) connect the median values in 1 bar IG CO_2.

Figure 4. Light microscopy of polished cross-sections after (a,c,e,g) 1000 h and (b,d,f,h) 2000 h exposures in 300 bar IG sCO_2 at 700°C (a-b) alloy 25, (c-d) 625, (e,f) 740H and (g,h) 282.

Figure 5. Light microscopy of polished cross-sections after (a,c,e,g) 1000 h and (b,d,f,h) 4000 h exposures in 300 bar IG sCO_2 at 750°C (a-b) alloy 25, (c-d) 625, (e,f) 740H and (g,h) 282.

Figure 6. Arrhenius plot of 300 bar IG CO_2 parabolic rate constants (solid symbols) compared to 750°C 1 bar IG CO_2 rate constants (open symbols). All of the rates are well below the metric established for the 100,000 h lifetime except for alloy 25 in 10-h cycles at 700° and 750°C.

Figure 7. Light microscopy of polished cross-sections after 2,500 h in (a,c,e,g) 1 bar and (b,d,f,h) 300 bar IG sCO_2 at 750°C (a-b) alloy 25, (c-d) 625, (e,f) 740H and (g,h) 282.

Figure 8. STEM bright field images of the scale formed after 1000 h at 700°C on alloy 25 in (a) 300 bar sCO_2 and (b) laboratory air. The thin scale in both environments has a much larger recrystallization (rx) zone beneath it.

Figure 9. (a) STEM bright field image of the scale formed on alloy 25 after 1000 h at 700°C in 300 bar sCO_2, and (b) line profile from the line in (a) showing the C concentration.

Figure 10. (a) STEM bright field image of the scale formed on alloy 25 after 1000 h at 700°C in 300 bar sCO_2, and X-ray maps of (b) Cr, (c) O, (d) C, (e) Si, (f) Fe, (g) Mn and (h) Mo.

Figure 11. (a) STEM bright field image of the scale formed on alloy 25 after 1000 h at 700°C in laboratory air, and X-ray maps of (b) Cr, (c) O, (d) C, (e) Si, (f) Fe, (g) Mn and (h) Mo.

Figure 12. Line profiles across the scales formed on alloy 25 after 1000 h at 700°C in laboratory air and 300 bar sCO_2 showing the Cr, C and Si contents as a function of distance from the gas interface.

Figure 13. (a) STEM bright field image of the scale formed on alloy 625 after 1000 h at 750°C in 300 bar sCO_2, and (b) line profile from the line in (a).

Figure 14. (a) STEM bright field image of the scale formed on alloy 25 after 1000 h at 750°C in 300 bar sCO_2, and X-ray maps of (b) Cr, (c) O, (d) Al, (e) Ti, (f) C and (g) Ni.

Table 1. Chemical composition of the alloys measured by inductively coupled plasma and combustion analyses in mass%.

Table 1. Chemical composition of the alloys measured by inductively coupled plasma and combustion analyses in mass%.

Alloy	**Fe**	**Ni**	**Cr**	**Co**	**Mo**	**Al**	**Ti**	**Other**
Sanicro 25	42.6	25.4	22.3	1.5	0.2	0.03	0.02	3Cu,0.5Mn,0.2Si,0.5Nb,3.5W,0.2N
625	4.0	60.6	21.7	0.1	9.4	0.09	0.2	3.6Nb,0.2Si,0.1Mn
282	0.2	58.0	19.3	10.3	8.3	1.5	2.2	0.06Si,0.1Mn
740	1.9	48.2	23.4	20.2	0.3	0.8	2.0	2.1Nb,0.3Mn,0.5Si

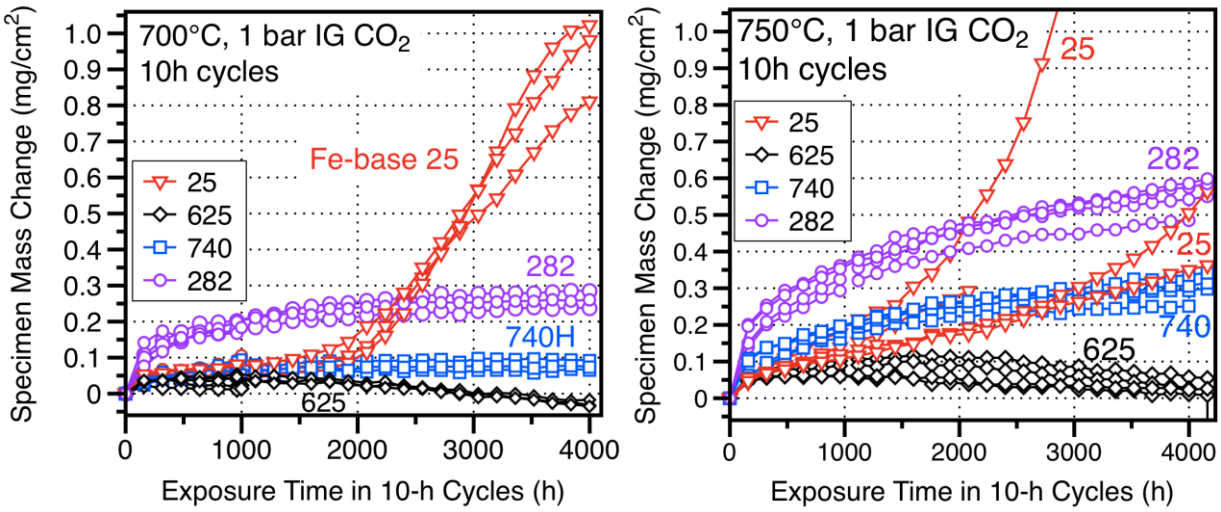

Figure 1. Specimen mass gain as a function of cumulative exposure time using 10-h cycles in 1 bar IG CO_2 at (a) 700°C (b) 750°C.

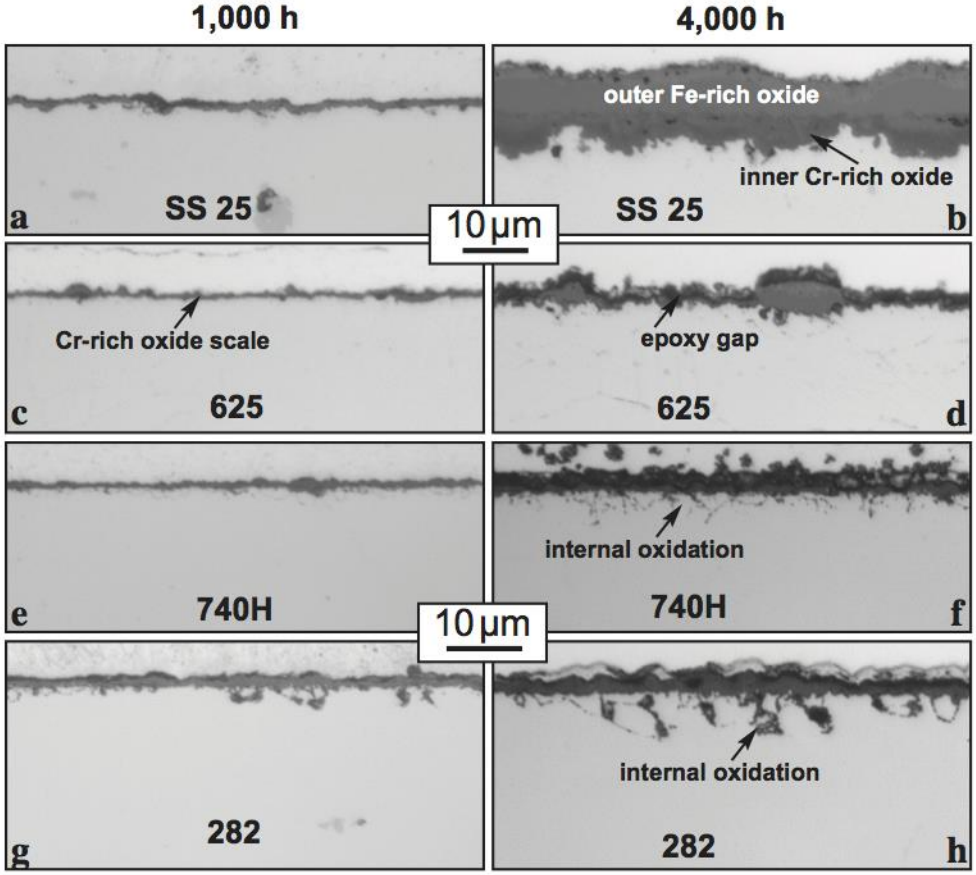

Figure 2. Light microscopy of polished cross-sections after (a,c,e,g) 1000 h and (b,d,f,h) 4000 h exposures in 1 bar IG CO_2 at 700°C (a-b) alloy 25, (c-d) 625, (e,f) 740H and (g,h) 282.

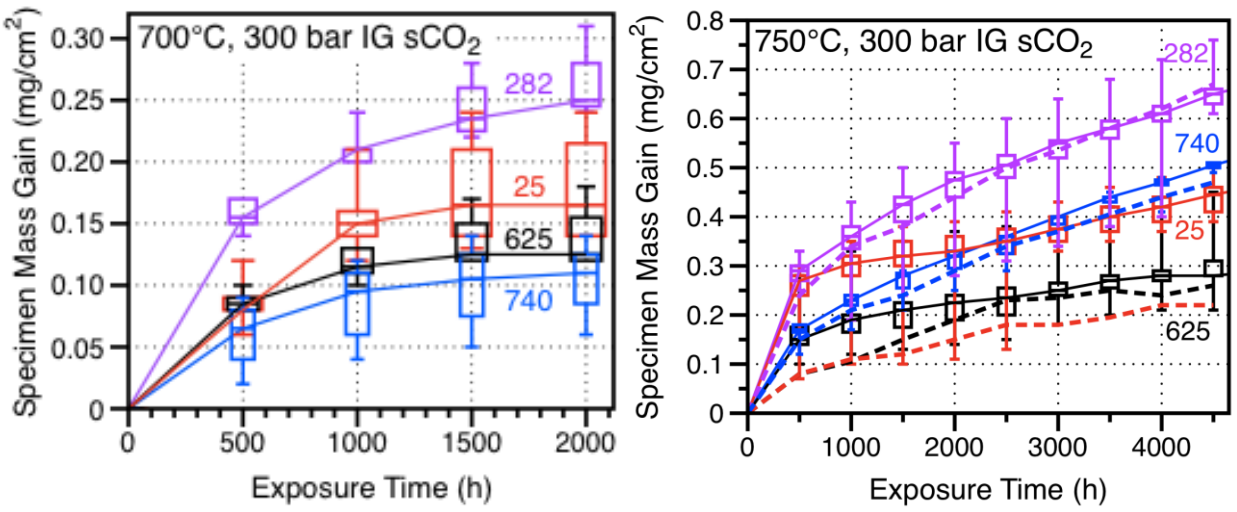

Figure 3. Specimen mass gain as a function of exposure time in 300 bar IG CO_2 at (a) 700°C and (b) 750°C. The whiskers show the maximum and minimum values measured for 6-10 specimens at each temperature and the boxes note the 25% and 75% values. The solid lines connect the median values. The dashed lines in (b) connect the median values in 1 bar IG CO_2.

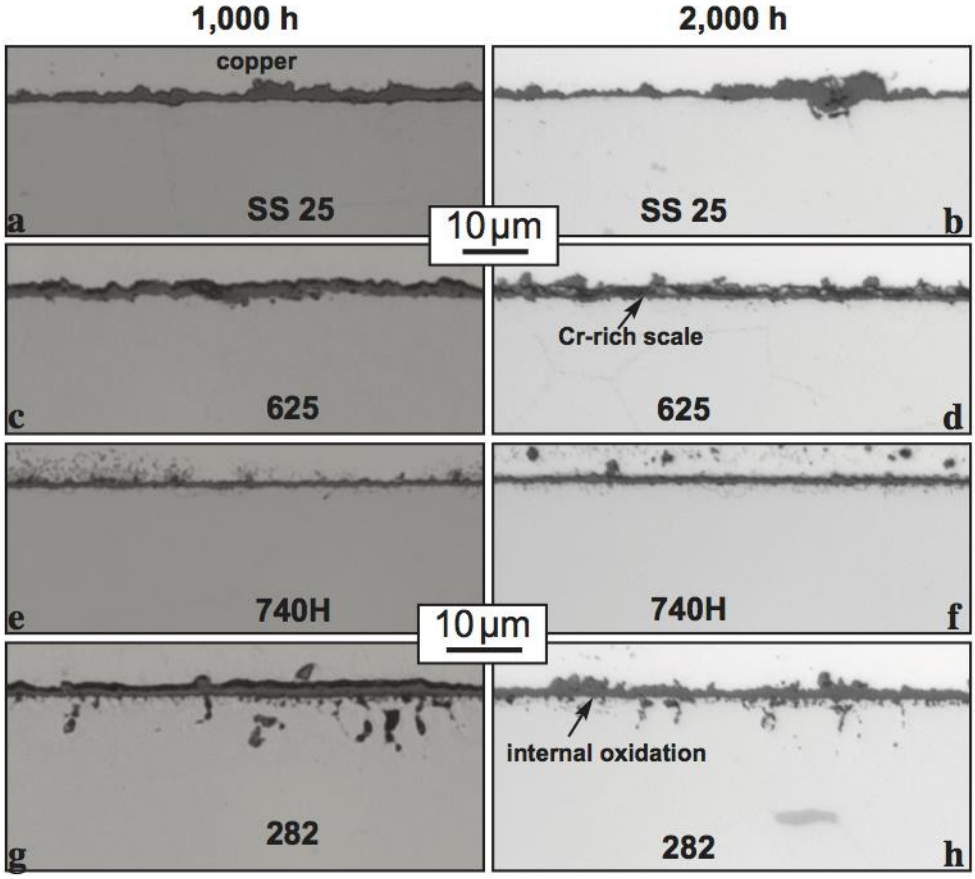

Figure 4. Light microscopy of polished cross-sections after (a,c,e,g) 1000 h and (b,d,f,h) 2000 h exposures in 300 bar IG sCO_2 at 700°C (a-b) alloy 25, (c-d) 625, (e,f) 740H and (g,h) 282.

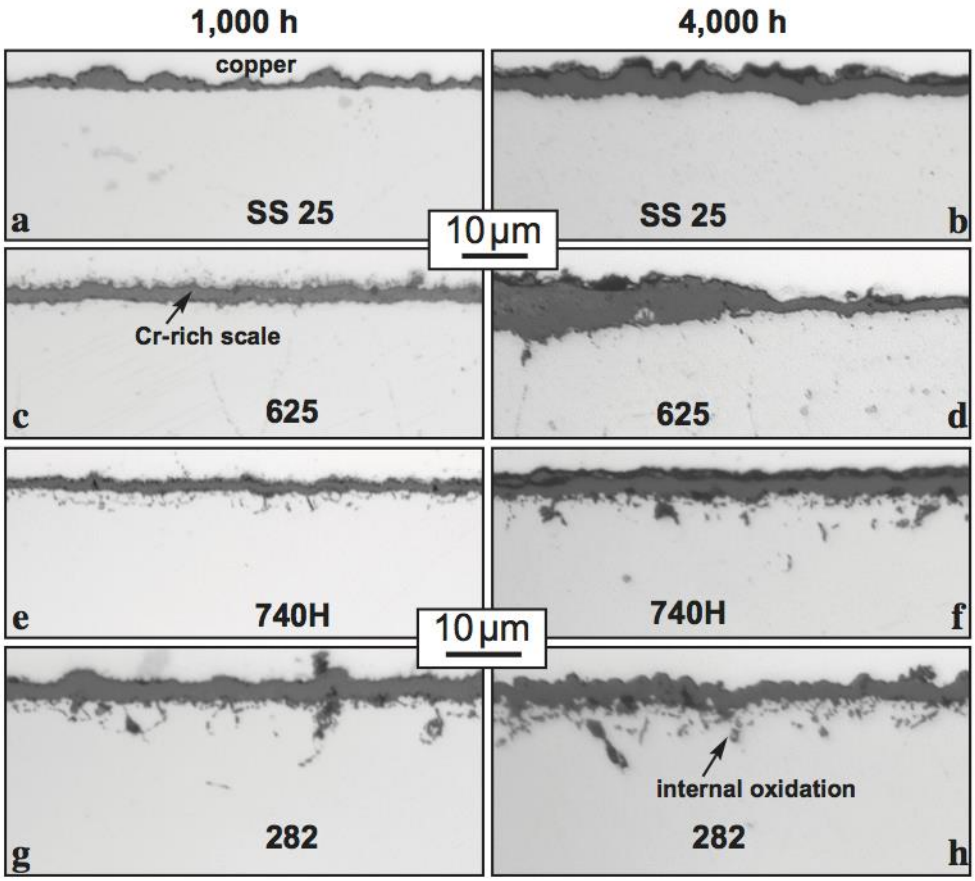

Figure 5. Light microscopy of polished cross-sections after (a,c,e,g) 1000 h and (b,d,f,h) 4000 h exposures in 300 bar IG sCO_2 at 750°C (a-b) alloy 25, (c-d) 625, (e,f) 740H and (g,h) 282.

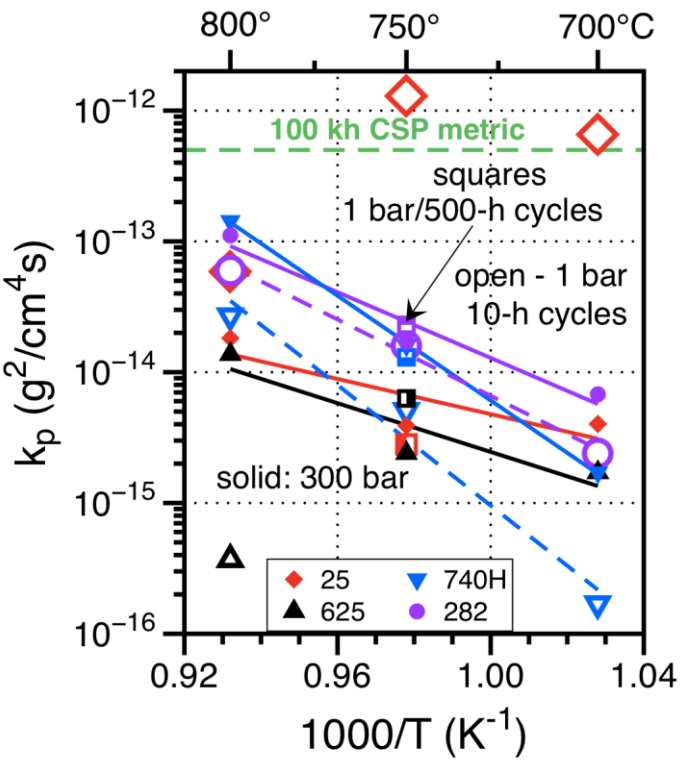

Figure 6. Arrhenius plot of 300 bar IG CO_2 parabolic rate constants (solid symbols) compared to 750°C 1 bar IG CO_2 rate constants (open symbols). All of the rates are well below the metric established for the 100,000 h lifetime except for alloy 25 in 10-h cycles at 700° and 750°C.

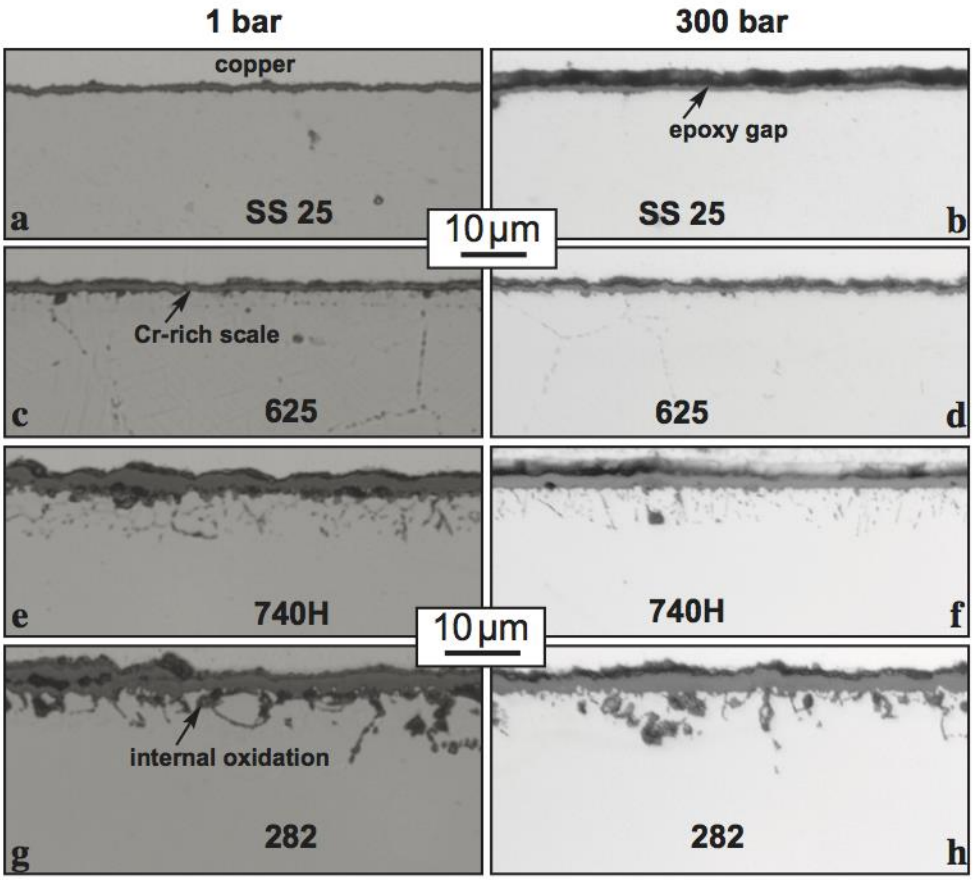

Figure 7. Light microscopy of polished cross-sections after 2,500 h in (a,c,e,g) 1 bar and (b,d,f,h) 300 bar IG sCO_2 at 750°C (a-b) alloy 25, (c-d) 625, (e,f) 740H and (g,h) 282.

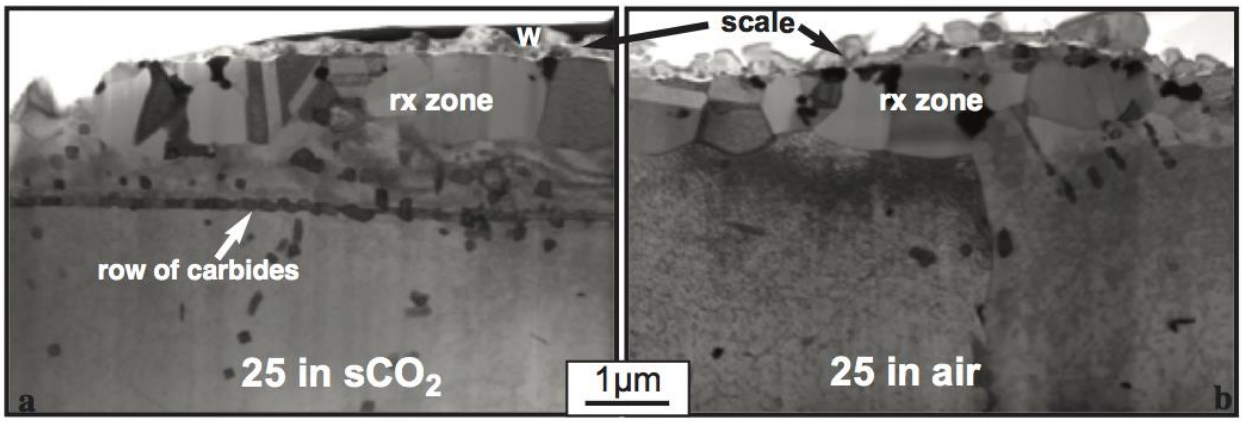

Figure 8. STEM bright field images of the scale formed after 1000 h at 700°C on alloy 25 in (a) 300 bar sCO_2 and (b) laboratory air. The thin scale in both environments has a much larger recrystallization (rx) zone beneath it.

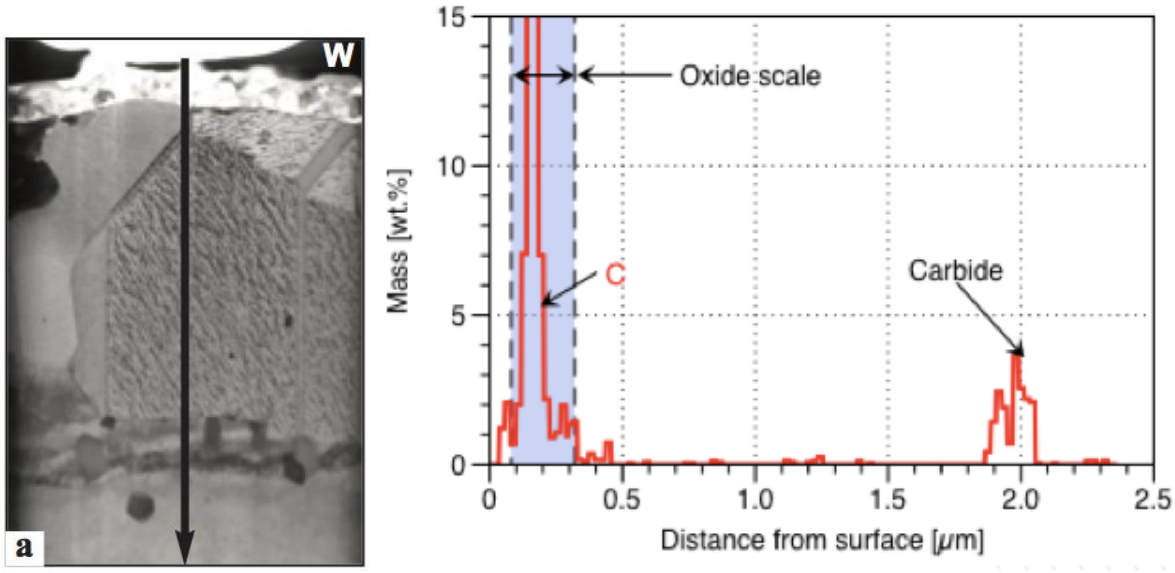

Figure 9. (a) STEM bright field image of the scale formed on alloy 25 after 1000 h at 700°C in 300 bar sCO_2, and (b) line profile from the line in (a) showing the C concentration.

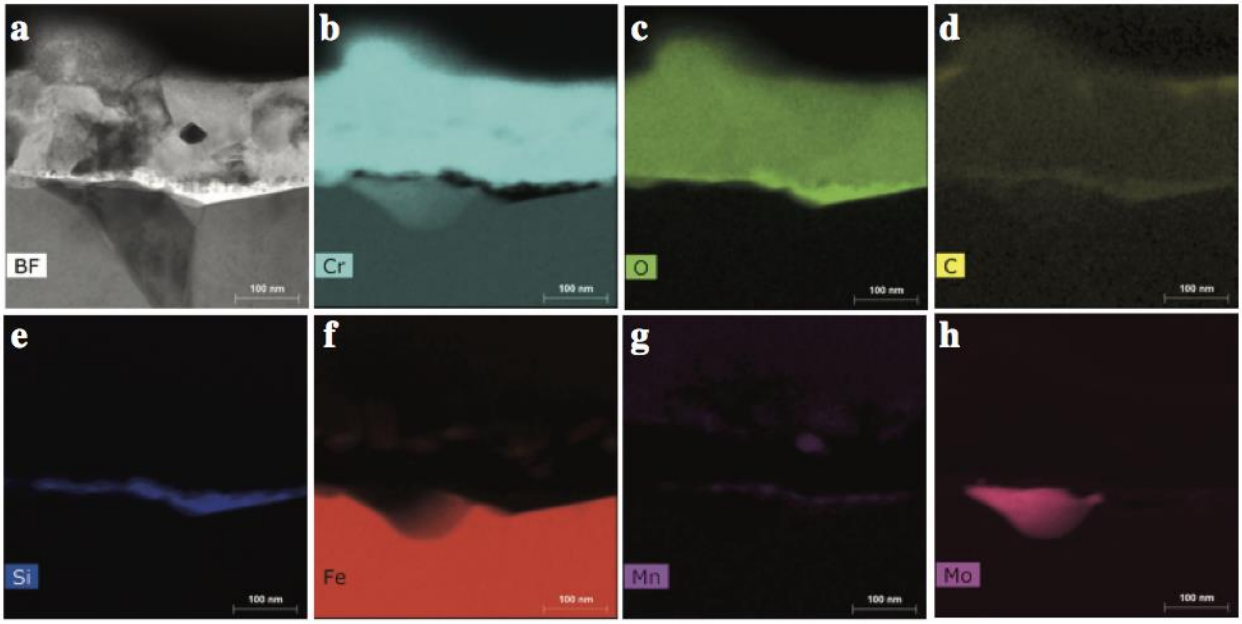

Figure 10. (a) STEM bright field image of the scale formed on alloy 25 after 1000 h at 700°C in 300 bar sCO_2, and X-ray maps of (b) Cr, (c) O, (d) C, (e) Si, (f) Fe, (g) Mn and (h) Mo.

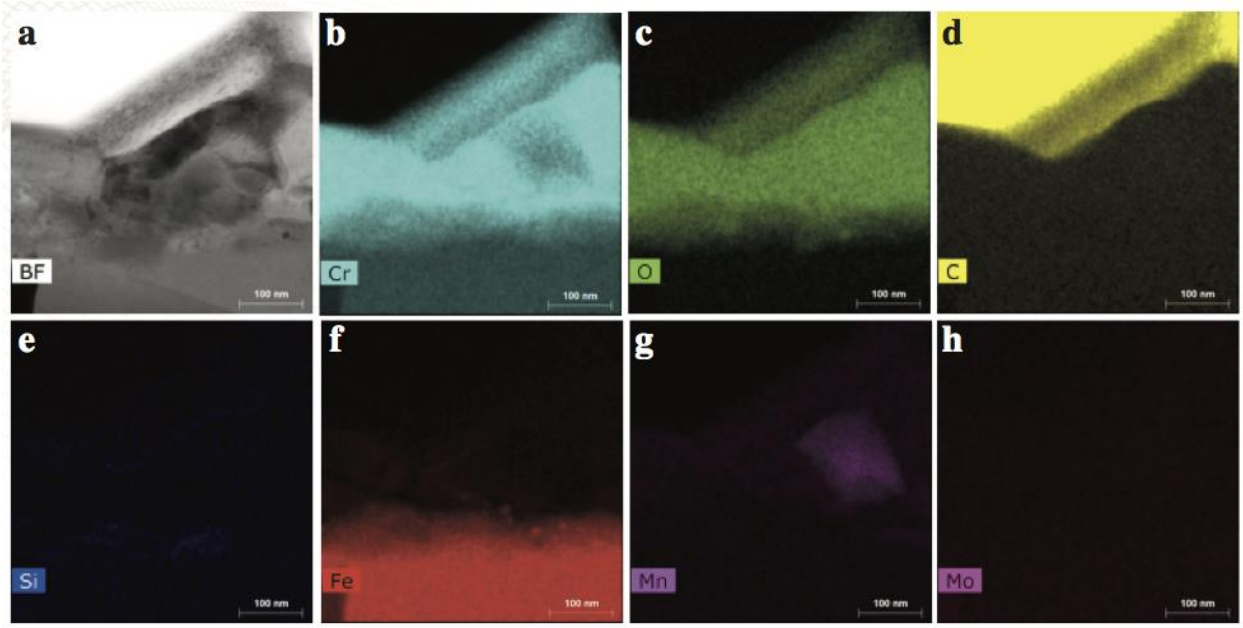

Figure 11. (a) STEM bright field image of the scale formed on alloy 25 after 1000 h at 700°C in laboratory air, and X-ray maps of (b) Cr, (c) O, (d) C, (e) Si, (f) Fe, (g) Mn and (h) Mo.

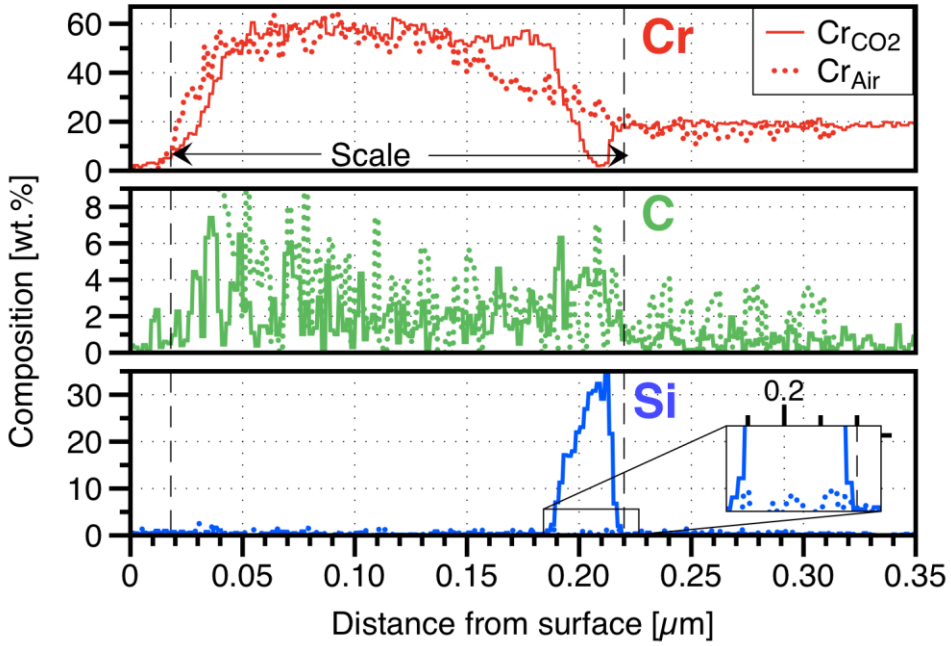

Figure 12. Line profiles across the scales formed on alloy 25 after 1000 h at 700°C in laboratory air and 300 bar sCO_2 showing the Cr, C and Si contents as a function of distance from the gas interface.

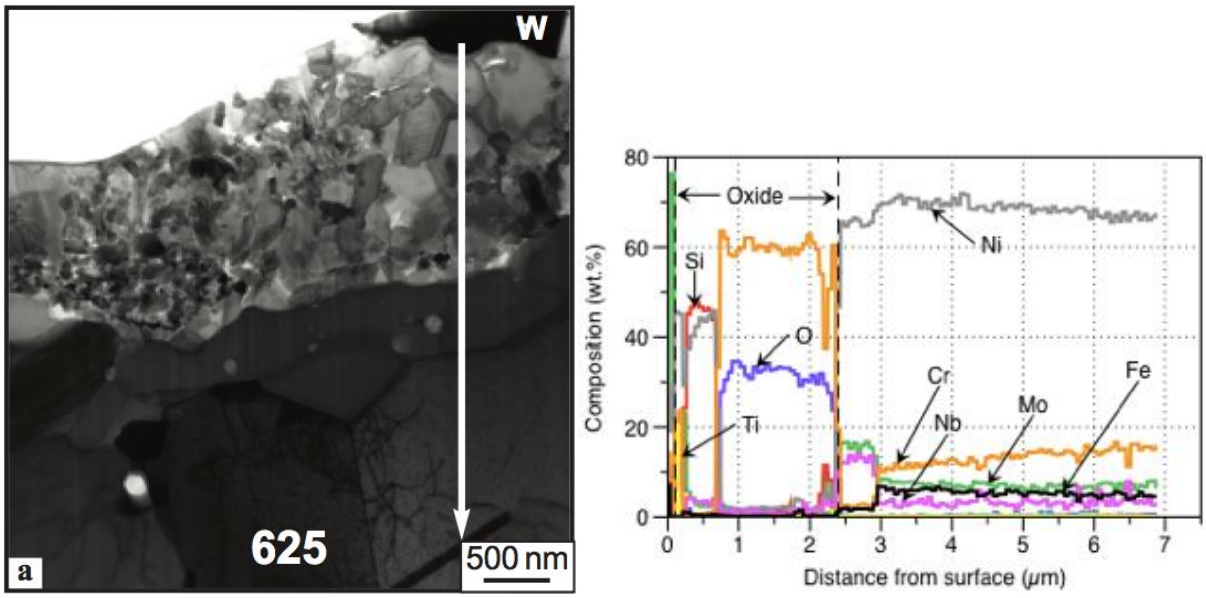

Figure 13. (a) STEM bright field image of the scale formed on alloy 625 after 1000 h at 750°C in 300 bar sCO_2, and (b) line profile from the line in (a).

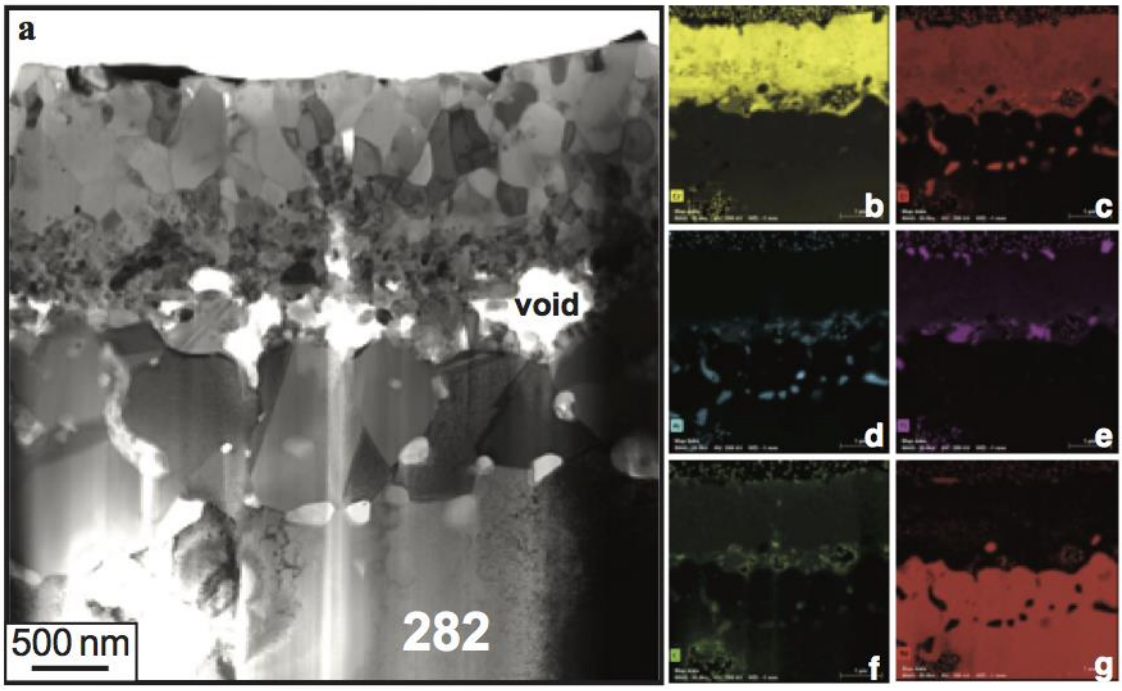

Figure 14. (a) STEM bright field image of the scale formed on alloy 25 after 1000 h at 750°C in 300 bar sCO_2, and X-ray maps of (b) Cr, (c) O, (d) Al, (e) Ti, (f) C and (g) Ni.

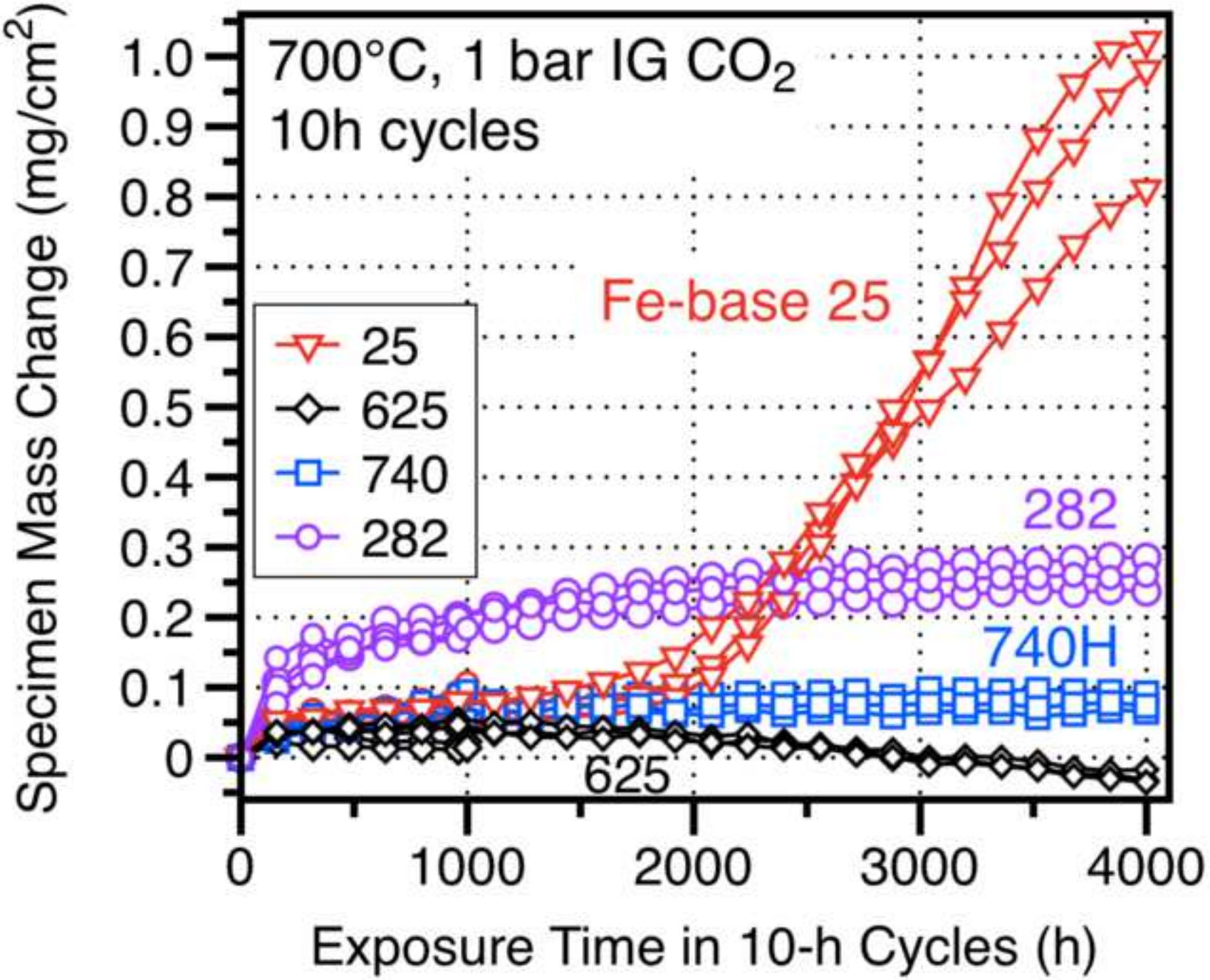

Colour figure (online version only)

Click here to download Colour figure (online version only) 1b. 75CX MoO.tiff

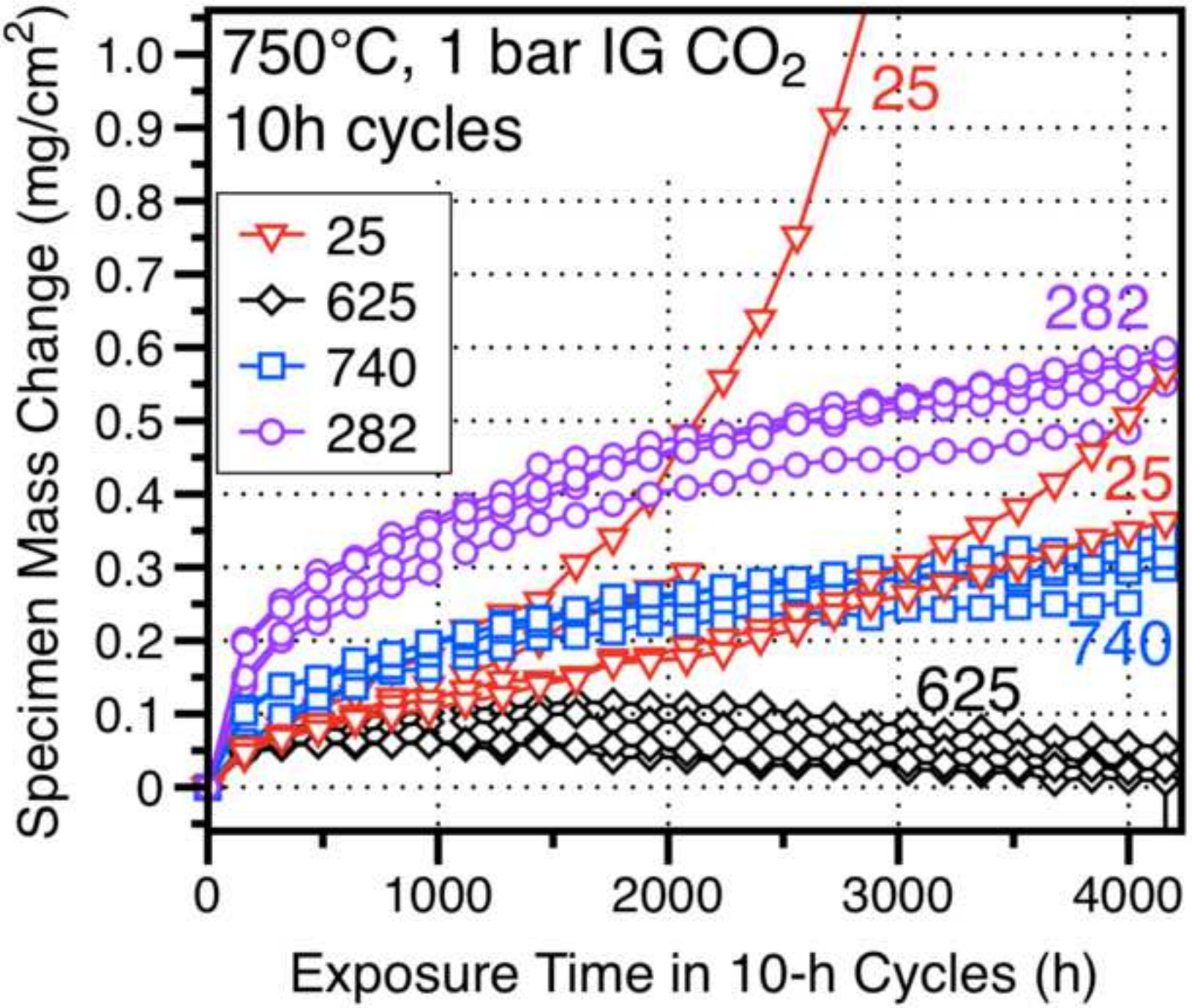

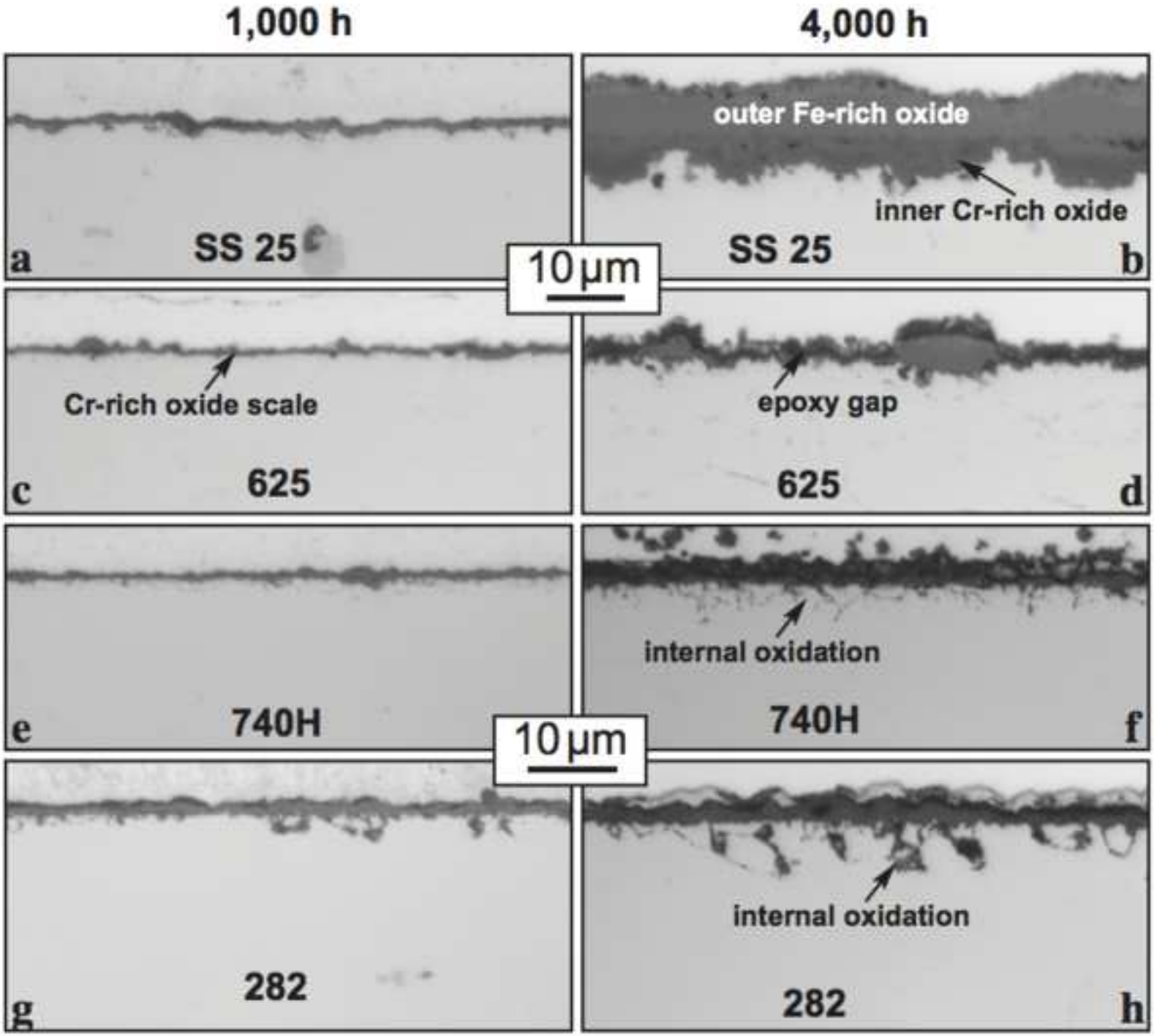

Colour figure (online version only)

Click here to download Colour figure (online version only) 3a. MoO 7SCL.tiff

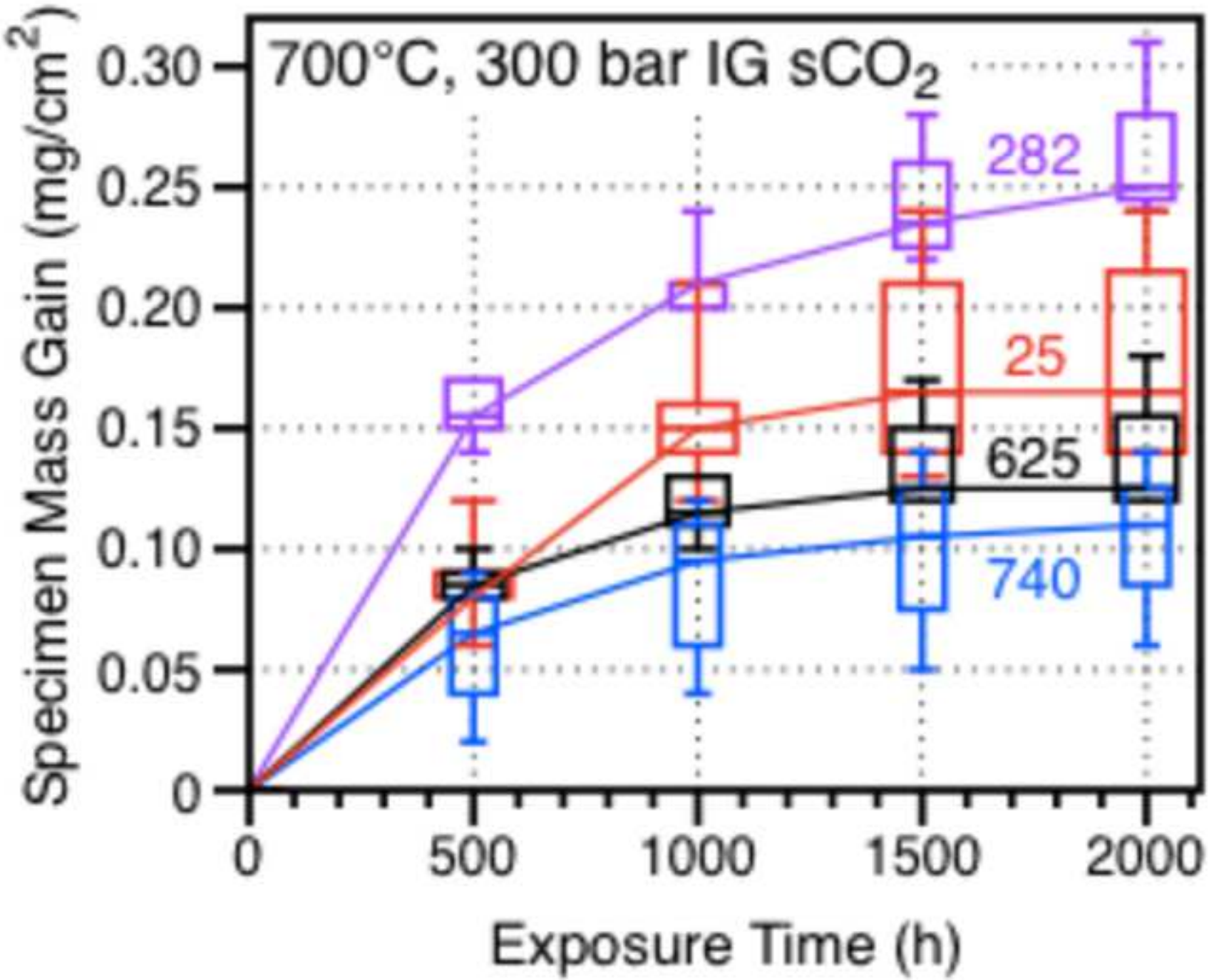

Colour figure (online version only)

Click here to download Colour figure (online version only) 3b. 75SCL MoO.tiff

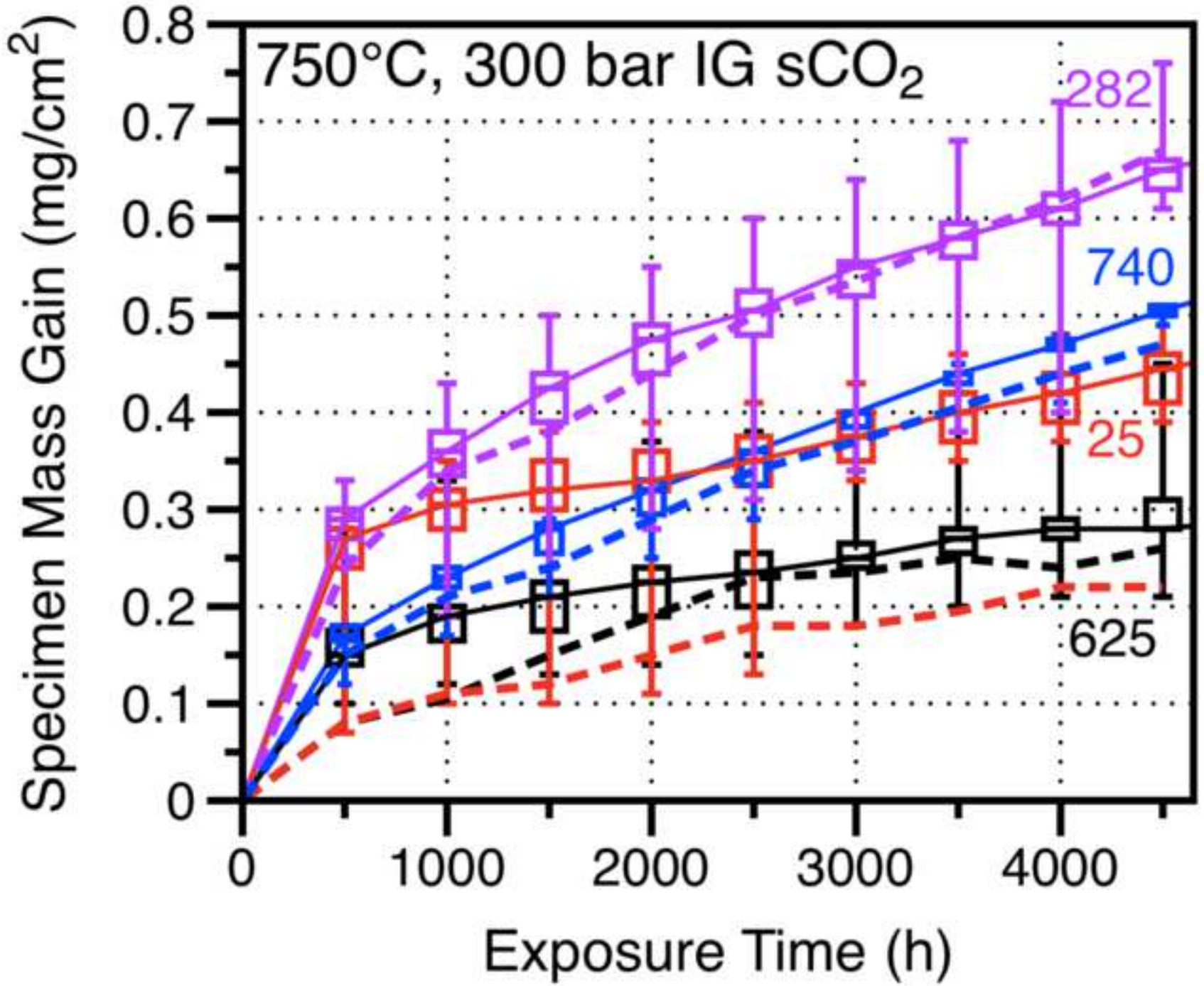

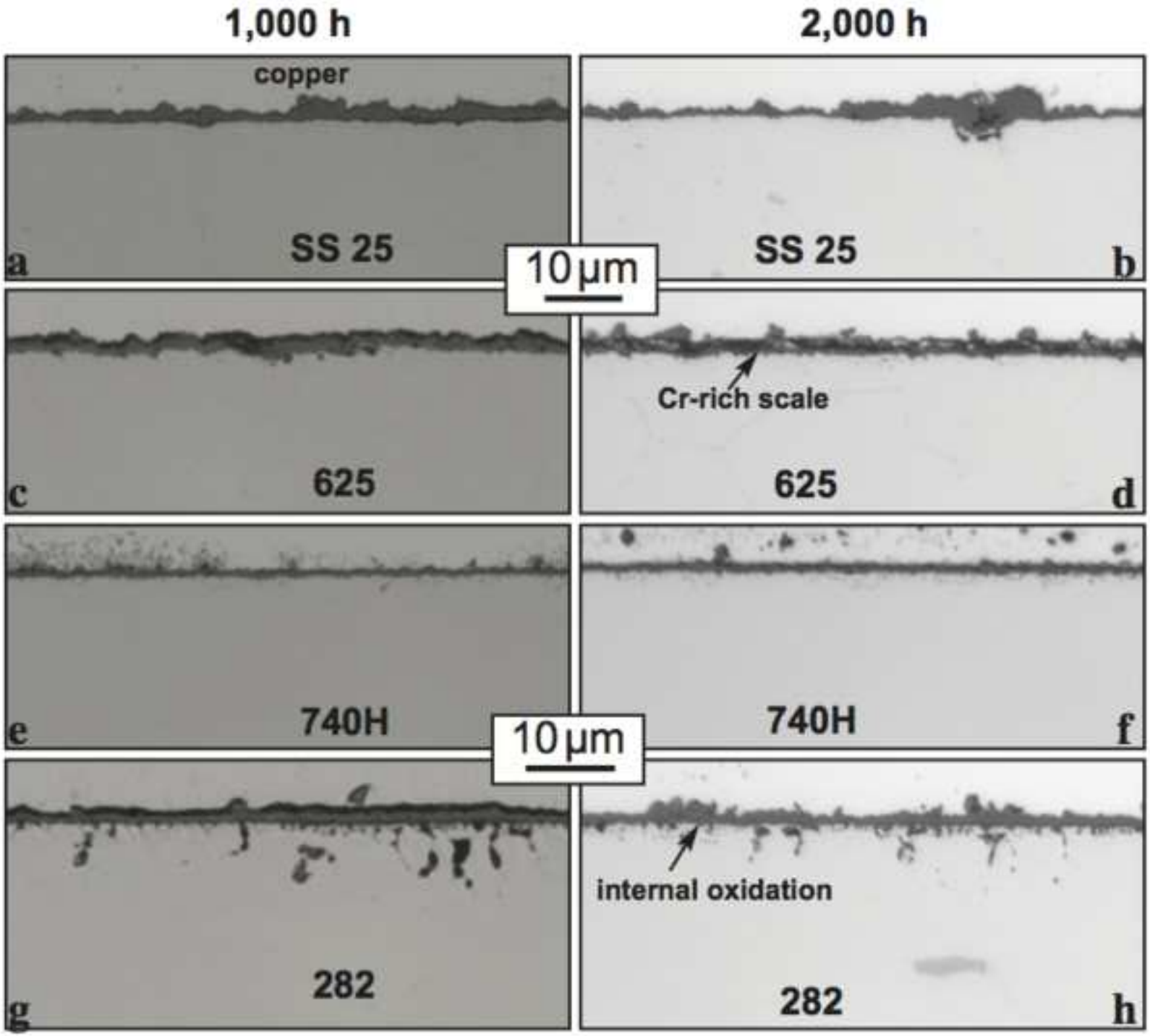

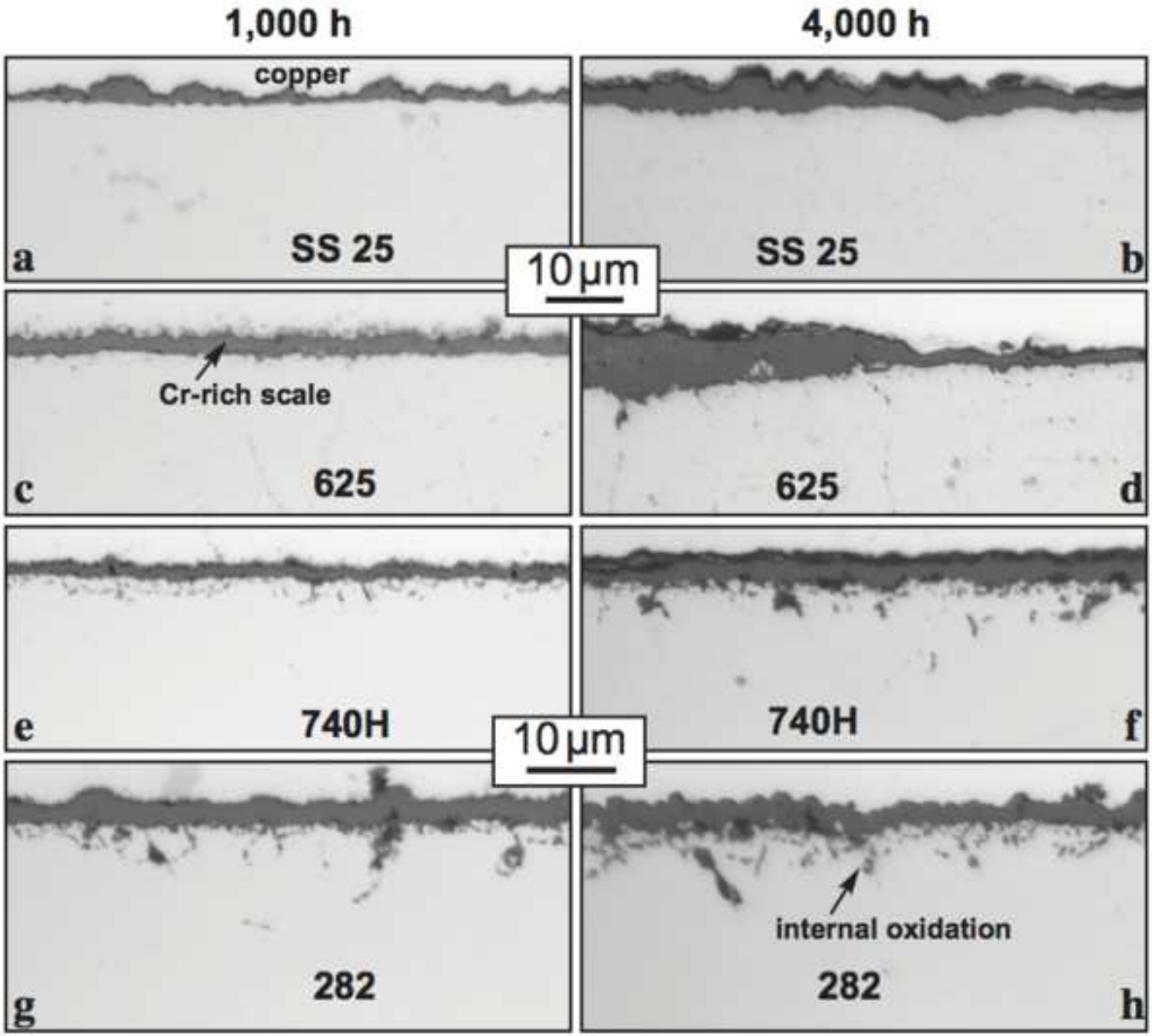

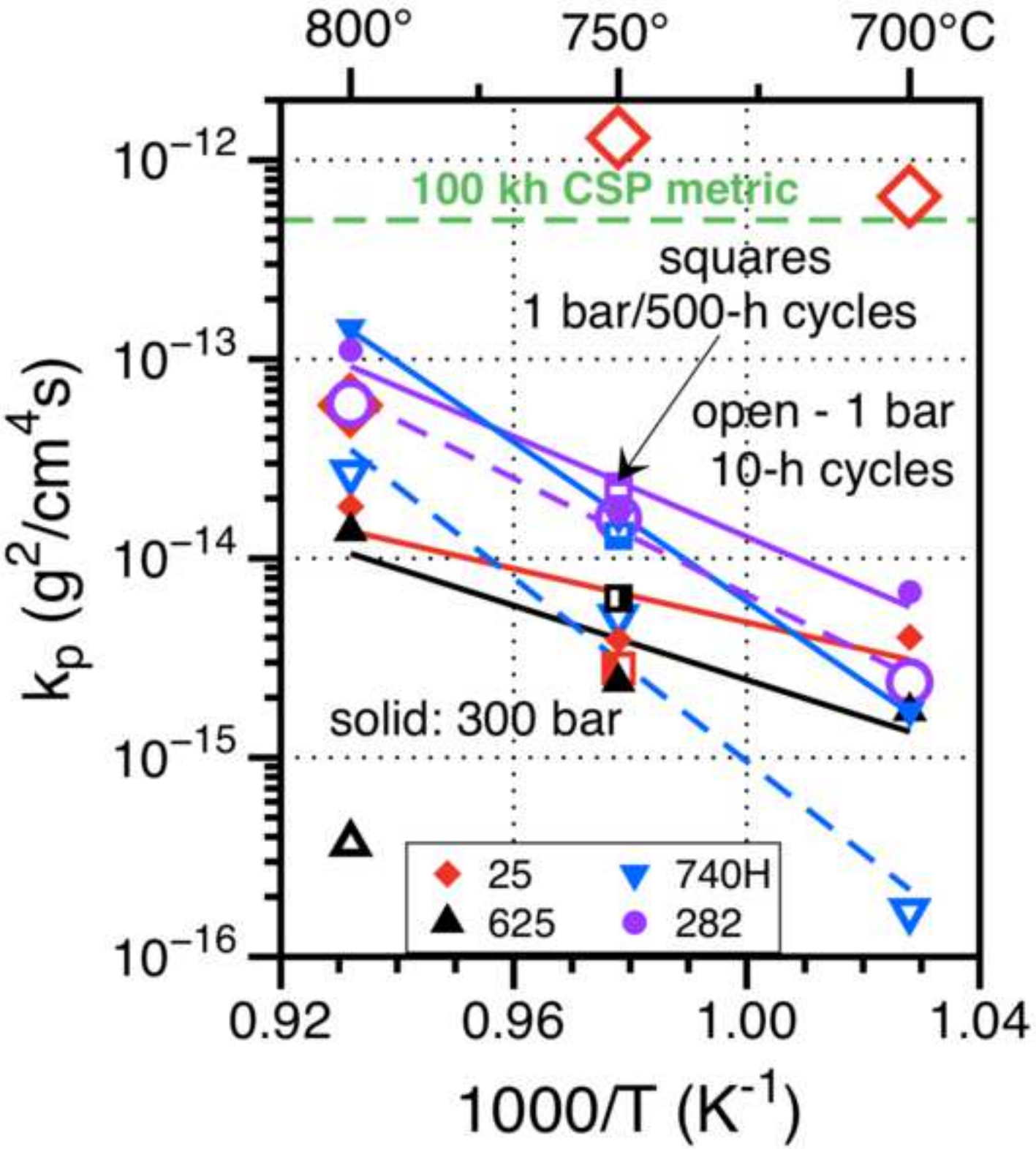

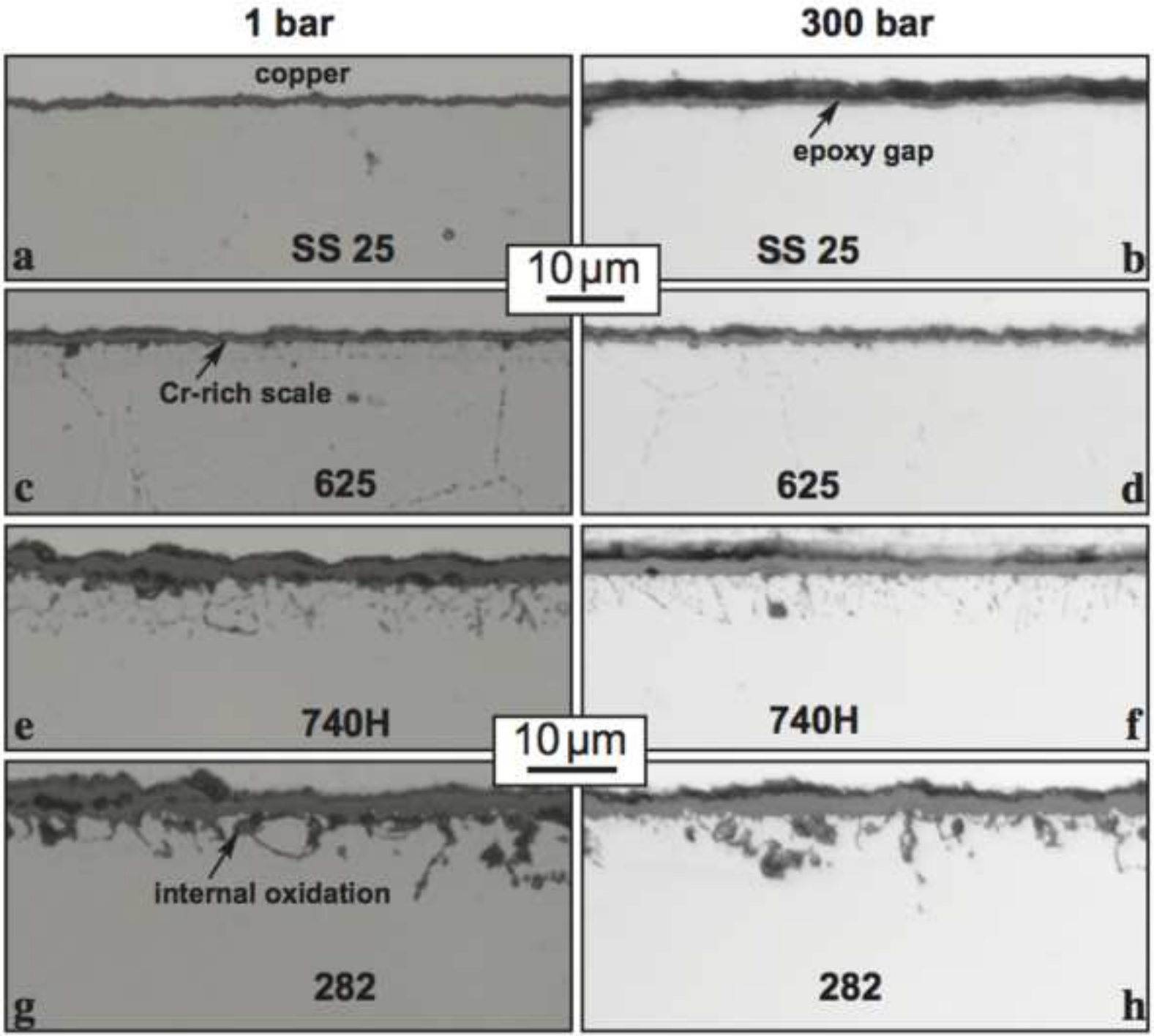

Non-colour figure

Click here to download Non-colour figure 8. TEM 25.png

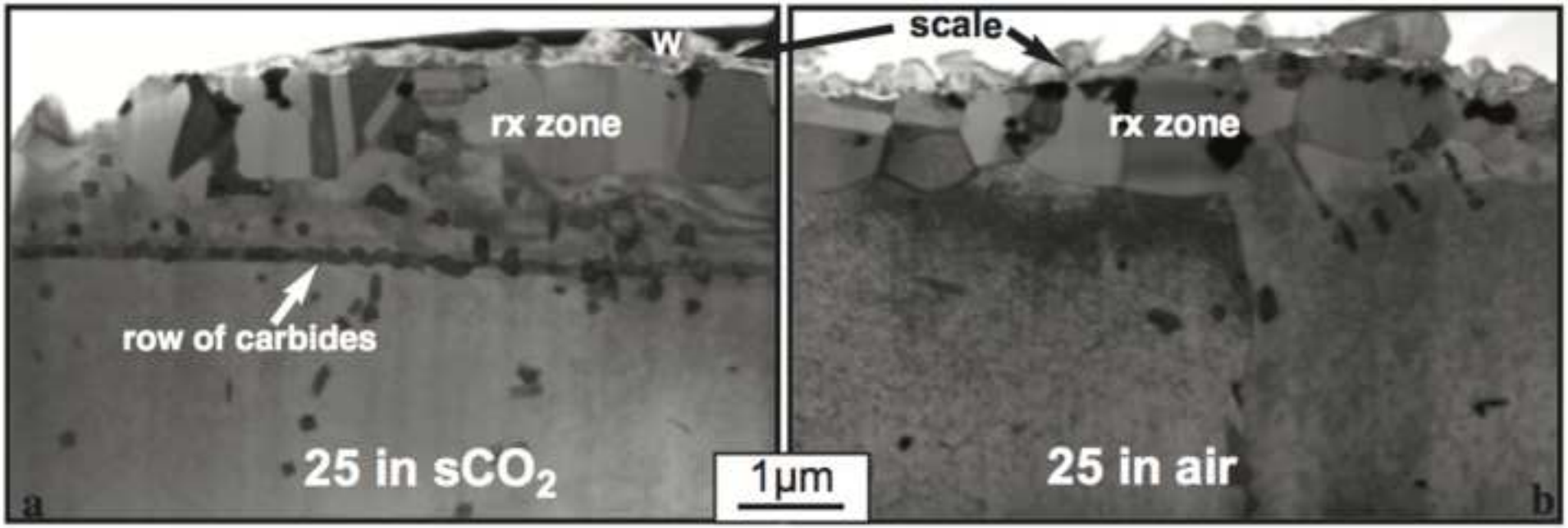

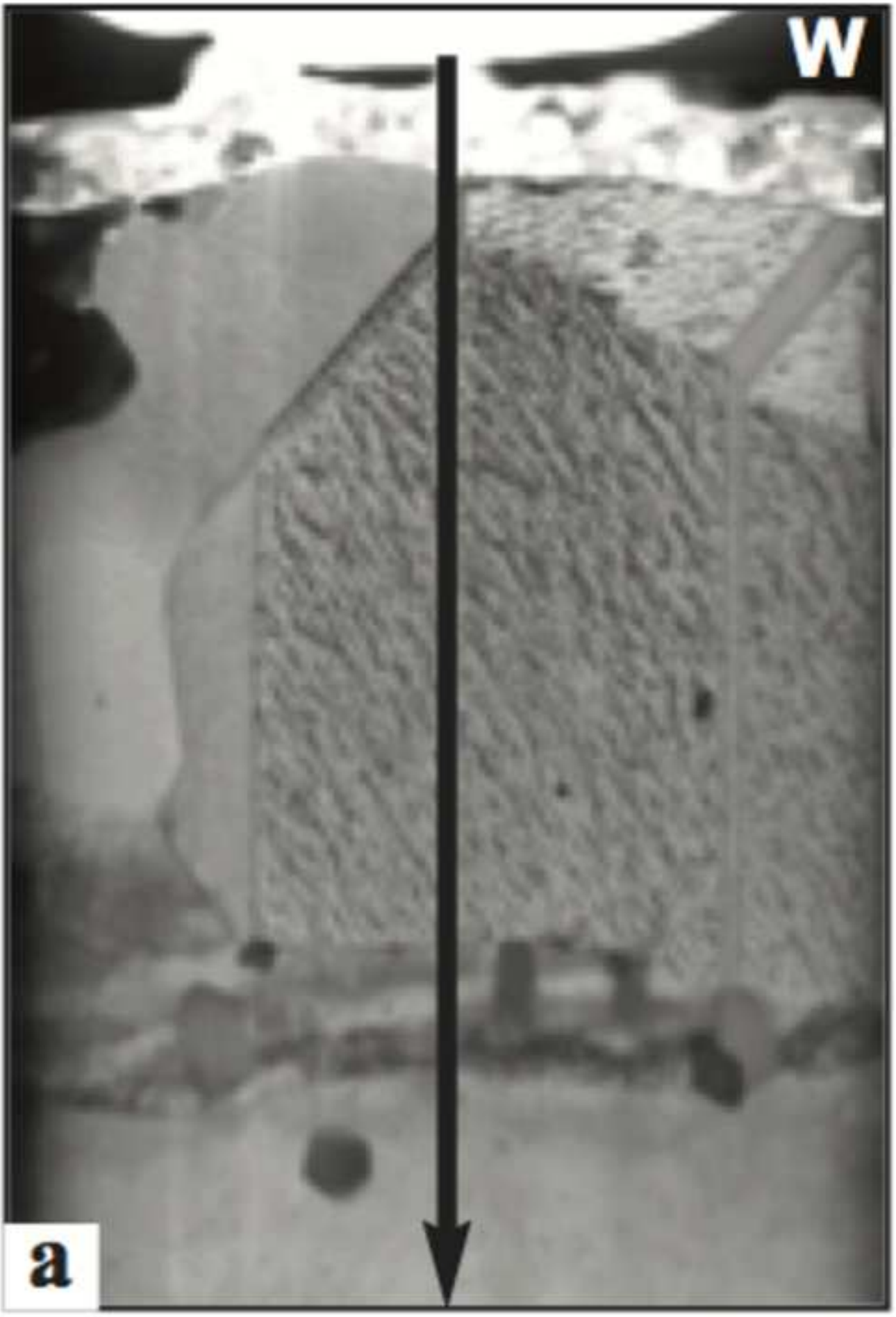

Colour figure (online version only)

Click here to download Colour figure (online version only) 9b. CSN25 line EDS.tiff

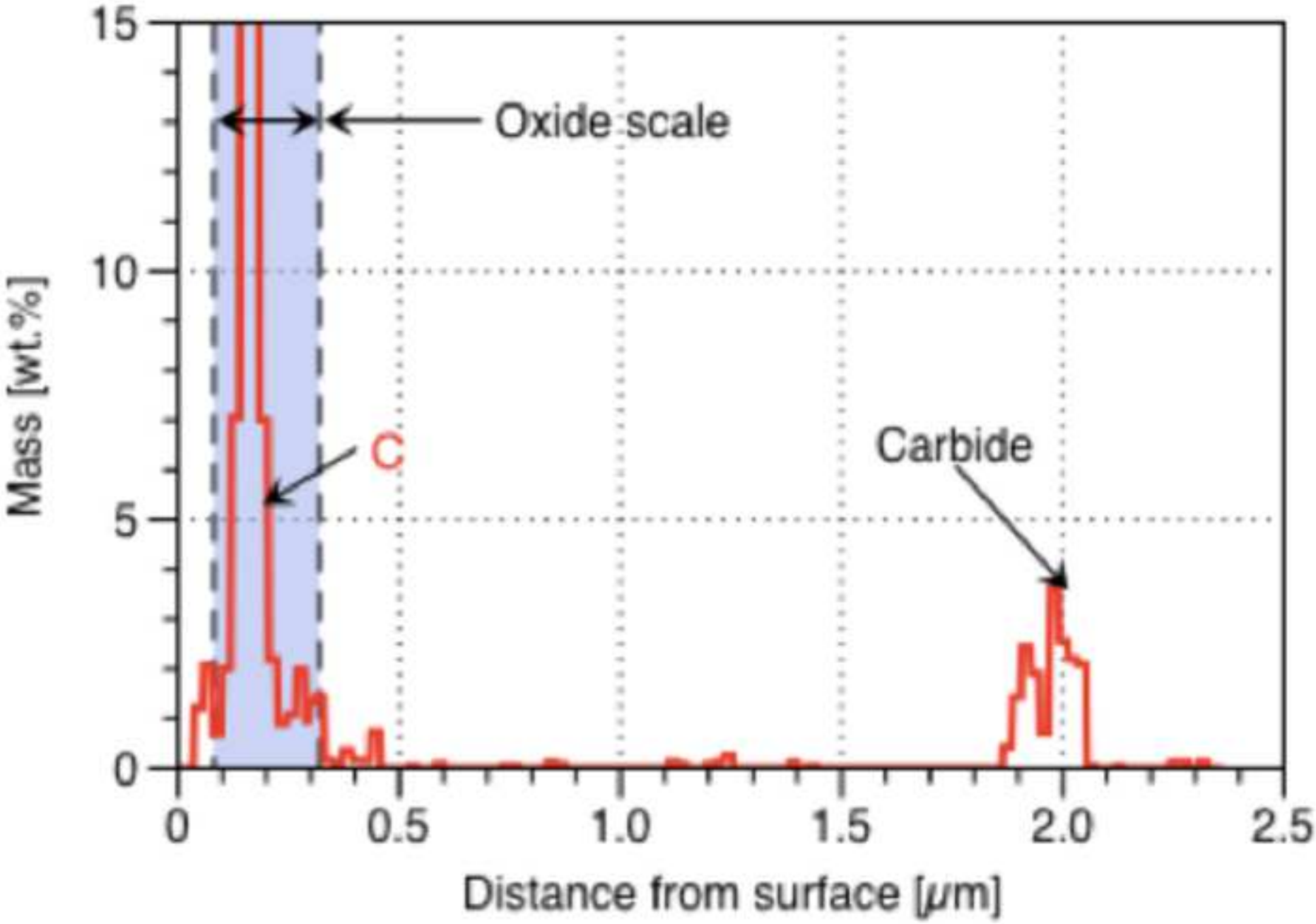

Colour figure (print)

Click here to download Colour figure (print) 10. 25 CO2 map.png

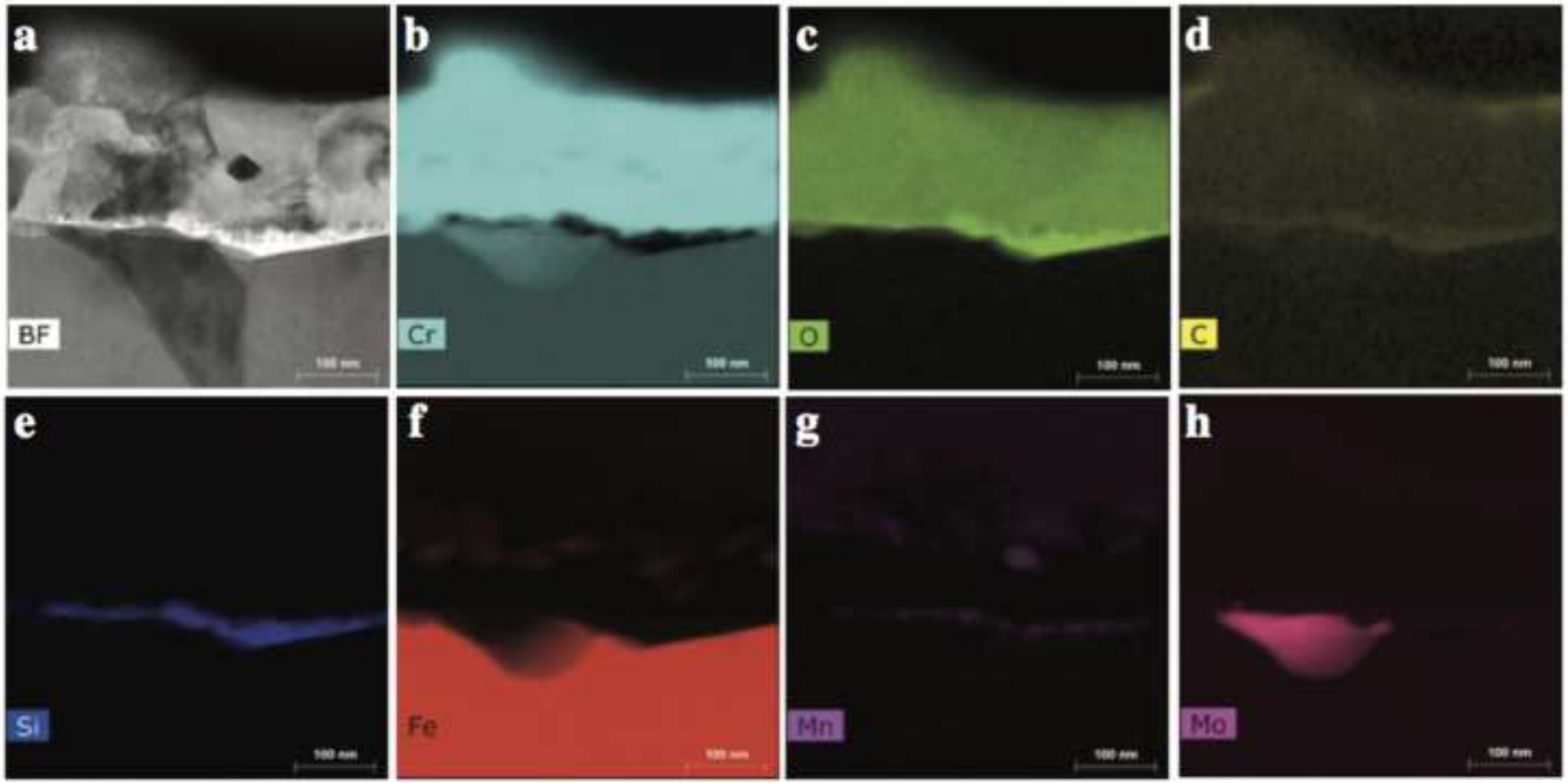

Colour figure (print)

Click here to download Colour figure (print) 11. 25 map.png

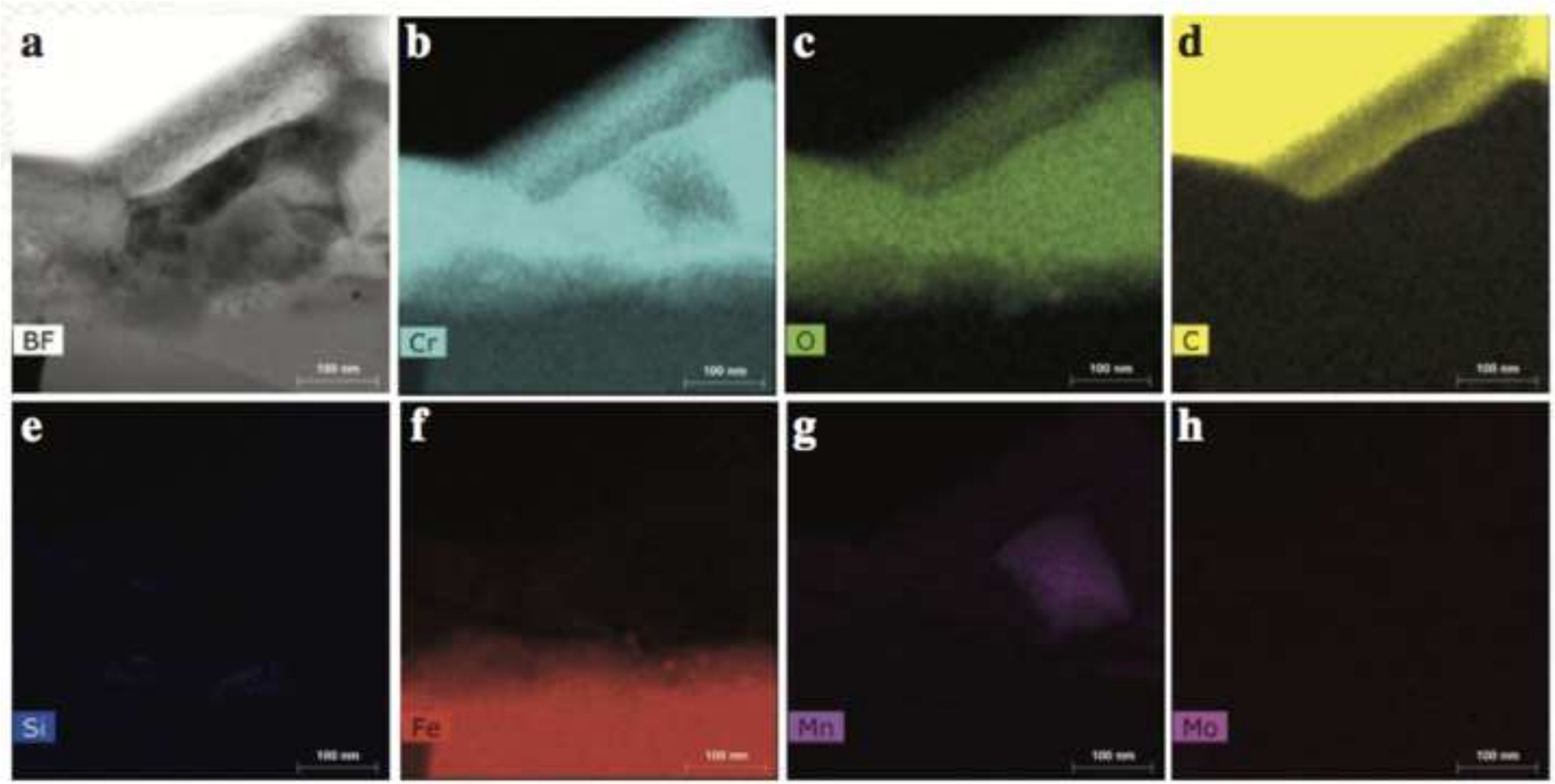

Colour figure (online version only)

Click here to download Colour figure (online version only) 12. SN25 STEM lines.tiff

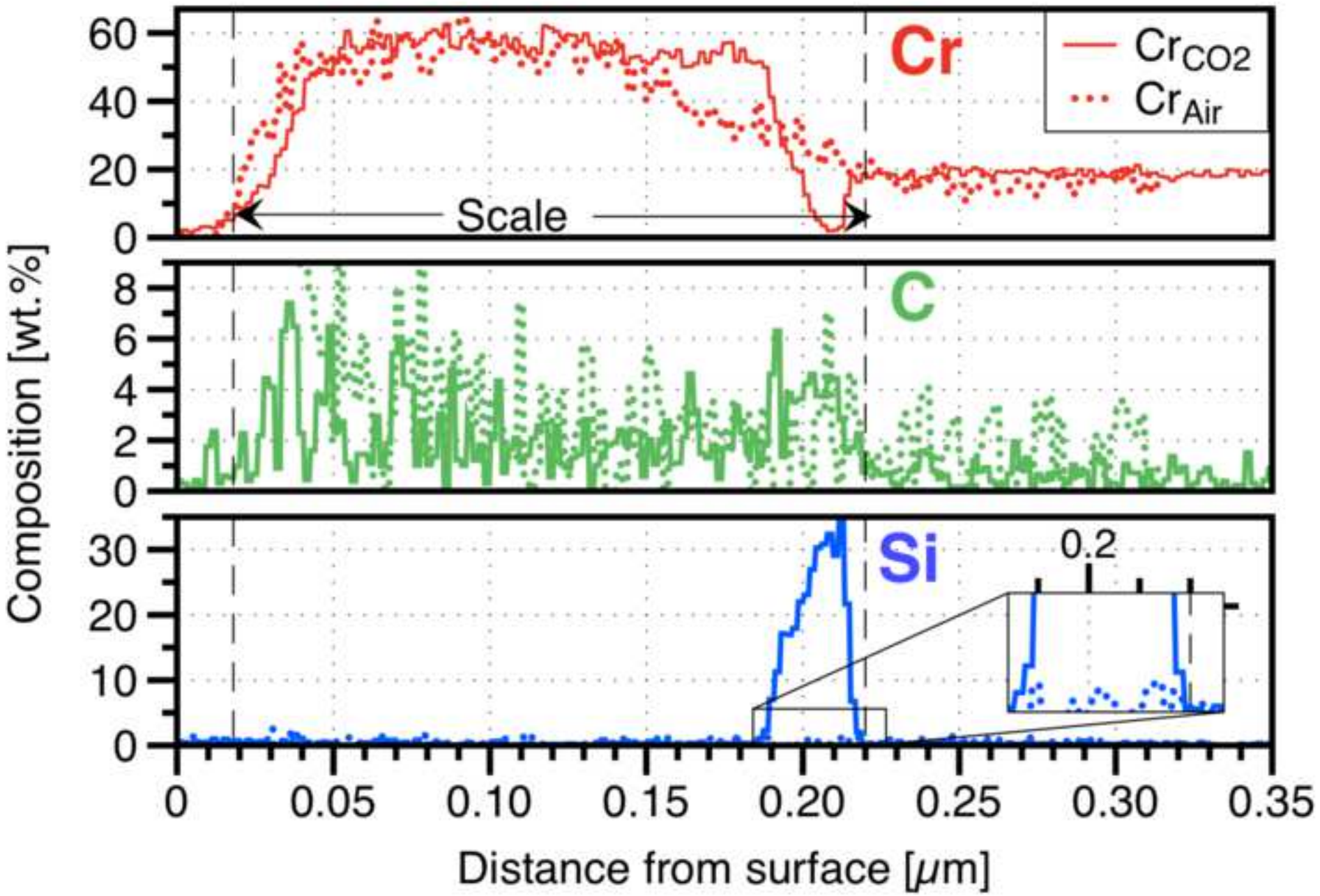

Non-colour figure

Click here to download Non-colour figure 13a 625 TEM.png

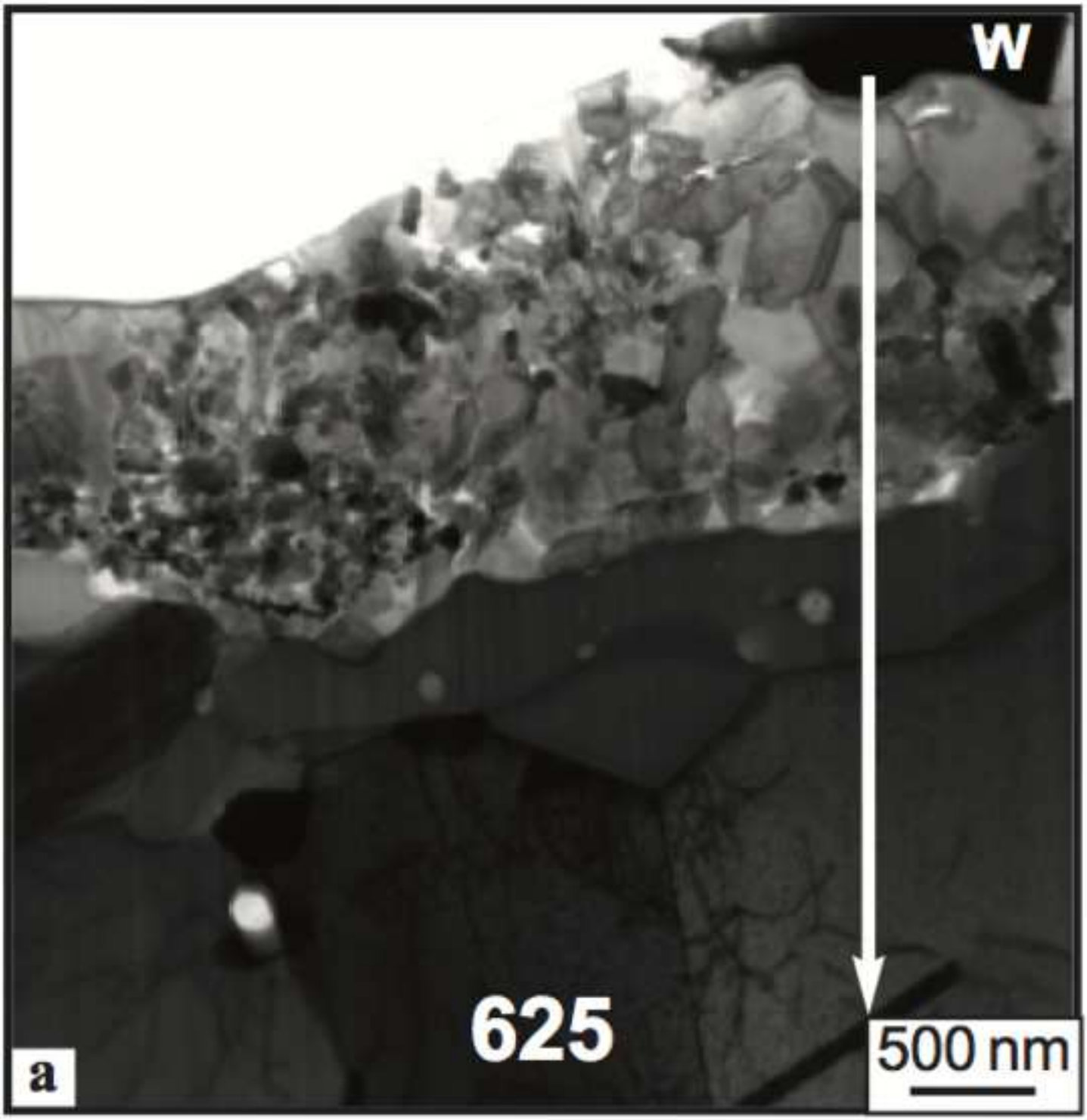

Colour figure (print)

Click here to download Colour figure (print) 13b C625 EDS line.tiff

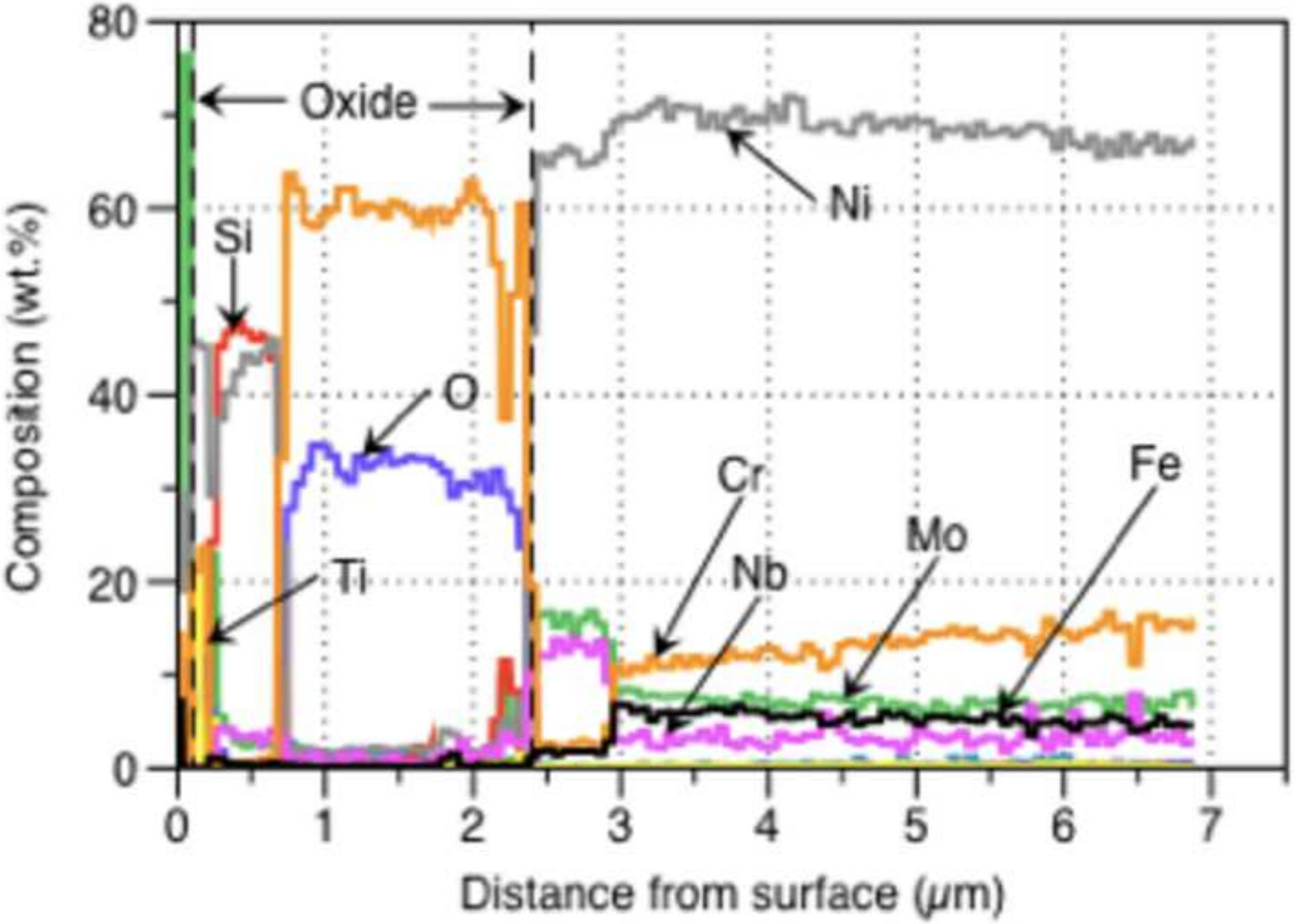

Colour figure (print)

Click here to download Colour figure (print) 14. 282 TEM.png